

# Remote sensing of lunar aureole with a sky camera: Adding information in the nocturnal retrieval of aerosol properties with GRASP code

R. Román<sup>a,b,c</sup>, B. Torres<sup>d,e</sup>, D. Fuertes<sup>e</sup>, V.E. Cachorro<sup>a</sup>, O. Dubovik<sup>d</sup>, C. Toledano<sup>a</sup>, A. Cazorla<sup>b,c</sup>, A. Barreto<sup>f,a,i</sup>, J.L. Bosch<sup>b,c,g</sup>, T. Lapyonok<sup>d</sup>, R. González<sup>a</sup>, P. Goloub<sup>d</sup>, M.R. Perrone<sup>h</sup>, F.J. Olmo<sup>b,c</sup>, A. de Frutos<sup>a</sup>, L. Alados-Arboledas<sup>b,c</sup>

<sup>a</sup>Atmospheric Optics Group (GOA), University of Valladolid (Spain)

<sup>b</sup>Department of Applied Physics, University of Granada. 18071, Granada (Spain)

<sup>c</sup>Andalusian Institute for Earth System Research (IISTA-CEAMA), University of Granada, Autonomous Government of Andalusia. 18006, Granada (Spain)

<sup>d</sup>Laboratoire d'Optique Atmosphérique, CNRS, Lille 1 University (France)

<sup>e</sup>Generalized Retrieval of Atmosphere and Surface Properties - SAS (France)

<sup>f</sup>Cimel Electronique, Paris, France

<sup>g</sup>Departamento Ingeniería Eléctrica y Térmica, University of Huelva (Spain)

<sup>h</sup>Dipartimento di Matematica e Fisica, Università del Salento, Lecce (Italy)

<sup>i</sup>Izaña Atmospheric Research Center, Meteorological State Agency of Spain, Izaña (Spain)

Correspondence to: R. Román (robertor@goa.uva.es)

## **Abstract**

The use of sky cameras for nocturnal aerosol characterization is discussed in this study. Two sky cameras are configured to take High Dynamic Range (HDR) images at Granada and Valladolid (Spain). Some properties of the cameras, like effective wavelengths, sky coordinates of each pixel and pixel sensitivity, are characterized. After that, normalized camera radiances at lunar almucantar points (up to  $20^\circ$  in azimuth from the Moon) are obtained at three effective wavelengths from the HDR images. These normalized radiances are compared in different case studies to simulations fed with AERONET aerosol information, giving satisfactory results. The obtained uncertainty of normalized camera radiances is around 10% at 533 nm and 608 nm and 14% for 469 nm. Normalized camera radiances and six spectral aerosol optical depth values (obtained from lunar photometry) are used as input in GRASP code (Generalized Retrieval of Aerosol and Surface Properties) to retrieve aerosol properties for a dust episode over Valladolid. The retrieved aerosol properties (refractive indices, fraction of spherical particles and size distribution parameters) are in agreement with the nearest diurnal AERONET products. The calculated GRASP retrieval at night time shows an increase in coarse mode concentration along the night, while fine mode properties remained constant.

## **Keywords**

Sky camera, Moon, GRASP, Aerosol, High Dynamic Range.

## 1.-Introduction

Aerosols have an important impact on the weather and climatic system and their contribution to the total radiative forcing estimation remains as the most uncertain [IPCC, 2014]. Depending on their properties, aerosols can increase the cooling or warming of the Earth surface by two mechanisms [Haywood and Boucher, 2000; Lohmann and Feichter, 2005]: the direct extinction (scattering and absorption) of solar and thermal radiation (direct effect), and acting as cloud droplet nuclei that leads to changes in the cloud properties and lifetime (indirect effect).

At night there is no solar radiation, but aerosol radiative forcing in the longwave range can be significant for large particles like desert dust and sea salt [Stier et al., 2007; Sicard et al., 2014]. In addition, at night the aerosol indirect effect still works and could provide changes on nocturnal cloud properties [Ramanathan et al., 2001; Kaufman et al. 2005; Rosenfeld et al. 2006]. These changes could contribute to global warming since clouds at night absorb part of the longwave radiation emitted by Earth, and then, they re-emit radiation back to the Earth surface [Ramanathan et al., 1989; NASA Facts, 1999; Wild, 2012]. Moreover, the knowledge of aerosol properties at night is important for the aerosol characterization in polar areas and in winter seasons, which present low sunshine duration values [Stone et al., 2010; Tomasi et al., 2015].

Some instruments and techniques are used for the characterization of aerosol properties at night: lidar systems provide backscatter and extinction profiles using Klett-Fernald-Sasano retrievals [Klett, 1981, 1985; Fernald, 1984; Sasano, 1984] and Raman measurements [Ansmann et al., 1990]; in-situ equipment can provide an accurate aerosol characterization but only for the local point where it is installed and not for the whole atmospheric column [McMurry et al., 2000; Rodríguez et al., 2012]; star and

lunar photometry provides aerosol optical depth (AOD) at different wavelengths [Ansmann et al., 2001; Pérez-Ramírez et al., 2008, 2011; Berkoff et al., 2011; Barreto et al., 2013, 2016, 2017]. The AOD measurements at night provide information to discriminate between the extinction of fine and coarse mode [O'Neill et al., 2003]. They are also useful for obtaining a reliable characterization of the fine mode properties, though the characterization of the coarse mode is less accurate [Torres et al., 2016].

Spectral AOD together with sky radiance provides adequate information to retrieve aerosol microphysical/optical properties (absorption and scattering) during daytime [Dubovik and King, 2000]. That is the case of the AERONET network (AErosol RObotic NETwork; <http://aeronet.gsfc.nasa.gov>), which provides these diurnal properties from sun/sky photometers distributed around the world [Holben et al., 1998]. At night, the sky radiances near the Moon (lunar aureole) could be used as a source of aerosol scattering information, at least between quarters when the Moon is brighter. This information could be combined with the spectral AOD, also obtained from the Moon (lunar photometry) to retrieve aerosol characteristics.

A sky camera can be used to obtain relative sky radiance near the Moon since it records the full hemispherical sky radiance measuring different wavelength intervals and it can operate at night with an appropriate exposure time (ET). It should be noted also that sky cameras usually present a low signal to noise ratio. Cloud detection is the most spread use of sky cameras [Long et al., 2006; Calbó and Sabburg, 2008; Cazorla et al., 2008a; Ghonima et al., 2012; Kazantzidis et al., 2012; Mandat et al., 2014, Alonso et al., 2014] though they have been used with other purposes [Horváth et al., 2002; Cazorla et al., 2008b; Kreuter et al., 2009; Sigernes et al., 2014], including the retrieval of sky radiances in daytime [Voss and Zibordi, 1989; López-Alvarez et al., 2008; Román et al., 2012; Toshing et al., 2013; Chauvin et al., 2015].

The main goal of this work is to propose and validate the use of sky cameras to obtain normalized radiances in the lunar aureole region. The secondary goal consists of using those normalized radiances as inputs in an inversion algorithm together with spectral AOD measurements (gained by lunar photometry) to retrieve aerosol properties during night time.

This paper is structured as follows: Section 2 presents the sites and instrumentation used in this work. The characterization of the sky camera and the methodology used to obtain normalized radiances are explained in Section 3. Section 4 introduces the GRASP code. A thorough comparison between normalized camera radiances and simulations is developed in Section 5. The GRASP inversion of camera radiances and AOD for a particular case is also shown in Section 5. Finally, Section 6 summarizes the main conclusions.

## **2 -Location and ancillary instrumentation**

The present work utilizes data from Granada and Valladolid (both located in Spain). Valladolid is an urban area, surrounded by rural areas, sited in North-Central Iberian Peninsula (150 km North from Madrid) with a population of ~300.000 inhabitants. Román et al. [2014b] characterized the predominant aerosol at Valladolid as “continental clean” obtaining monthly mean values of the AOD at 443 nm ranging from 0.10 to 0.24, and Angström Exponent (AE) from 0.9 to 1.5, showing higher/lower AOD/AE values in summer due to episodic Saharan dust events [Cachorro et al., 2016]. Granada, located in the South-East of the Iberian Peninsula, is a medium-sized and non-industrialized city situated in a natural basin surrounded by mountains and with a population similar to Valladolid; the local aerosol sources are mainly the heavy traffic

(particularly diesel vehicles) together with the re-suspension of material available on the ground, especially during the warm season. In winter, domestic heating (based on fuel oil combustion) also represents an important anthropogenic aerosol source [Lyamani et al., 2010; 2011; Titos et al., 2012; 2014]. AERONET provides a climatology table (Level 2.0) for Granada with monthly mean values of the AOD at 500 nm between 0.10 and 0.20 and AE values between 0.8 to 1.4, being AOD/AE values higher/lower in summer, also because of frequent Saharan dust outbreaks.

Both places are equipped with a “CHM-15k Nimbus” ceilometer (*Lufft* manufacturer), a “CE318-T” photometer (*Cimel Electronique*) and a “SONA” sky camera (*Sieltec Canarias S.L.*). One “CE318-N” photometer (*Cimel Electronique*) is also installed at Valladolid. These instruments are on the rooftop of the Science faculty of the University of Valladolid (41.66°N; -4.71°W; 705 m a.s.l.) and on the rooftop of the Andalusian Institute for Earth System Research (IISTA-CEAMA; 37.16°N; -3.61°W; 680 m a.s.l.). The mentioned ceilometers belong to the Iberian Ceilometer Network, ICENET, which processes raw data and provides information about the vertical attenuated backscatter at 1064 nm [Cazorla et al., 2017]. This information helps to detect possible changes in the aerosol properties at night.

The CE318-N photometer takes measurements of Sun irradiance and sky radiance, and CE318-T photometer also measures lunar direct irradiance, performing daytime and night time photometric measurements [Barreto et al., 2016]. The photometer #914 (CE318-T) was available for a short campaign at Valladolid and used in this work. For the rest of the period, the photometer #788 or the photometer #383 (both CE318-N), located at the same station, were used. Both photometers belong to the RIMA network (Iberian network for aerosol measurements), which is federated to AERONET. The #918 (CE318-T), used for this work at Granada, belongs to I-AMICA

(Infrastruttura di Alta Tecnologia per il Monitoraggio Integrato Climatico-Ambientale of Italy) and operates within AERONET. These instruments are periodically calibrated, following the AERONET protocol, ensuring high quality data. In addition, AERONET processes the photometer data providing a wide set of products such as daytime AOD at 8 wavelengths, aerosol size distribution, fraction of spherical particles (sphere fraction) and refractive indices [Holben et al., 1998; Dubovik et al., 2000, 2006]. Regarding night time measurements, AOD is obtained at 6 wavelengths (440, 500, 675, 870, 1020 and 1640 nm) following the method described in Barreto et al. [2016] which uses the ROLO (RObotic Lunar Observatory) model [Kieffer and Stone, 2005] for the lunar extraterrestrial irradiance calculation. ROLO is an empirically-based model that provides, for a given place and time, the spectral extraterrestrial lunar irradiance using the following geometrical variables: lunar phase angle; selenographic latitude and longitude of the observer; and selenographic longitude of the Sun. The calibration of the instrument for lunar measurements was done by the “Lunar Langley Method” explained by Barreto et al. [2013].

### **3- Sky camera**

SONA (“Sistema de Observación de Nubosidad Automático”: Automatic Cloud Observation System) sky camera is a device which provides full sky images at day and night. The system was mainly designed for cloud cover detection, but it can be used with other purposes. It is composed of a surveillance CCD camera with a fisheye lens inside a waterproof case and a dome with a shadow band blocking the Sun [González et al., 2012]. The CCD sensor provides RGB images with 8 bit-digitalization yielding 256 counts per channel [Cazorla et al., 2015]. The CCD resolution is 640x480 pixels, but the

system at Granada site was configured to record images of 480x480 pixels. An infrared (IR) cut-off filter is installed between the CCD and the fisheye lens in a mobile platform in order to block or to allow IR light into the sensor. Both cameras used in this paper were configured to take all images with the IR cut-off filter. The temperature (T) of the CCD is also logged with a resolution of 0.5°C.

### **3.1- Camera characterization**

#### **3.1.1- Effective wavelengths**

The CCD spectral response, given by the manufacturer, is shown in Fig. 1a. This response is only available up to 700 nm, but red channel seems to have certain sensitivity to longer wavelengths. As mentioned above, the camera also contains an IR cut-off filter to block the longest wavelengths. The spectral response of this filter, given by the manufacturer, is also shown in Fig. 1b. The filter transmittance can be considered constant and with a value about 90% from 400 nm up to 600 nm. At longer wavelengths, the transmittance starts to decrease, being ~50% at 640 nm and below 10% at 700 nm. The total spectral response of the sky camera is the CCD response weighted by the IR cut-off filter transmittance, shown at Fig. 1c. This total spectral response shows that the camera is not sensitive to infrared light above 700 nm, due to the effect of the IR cut-off filter, and presents its highest response in the green channel.

Sky radiance is measured in three broadband channels (Fig. 1c) but, as a first approximation, the radiance at these broadband channels can be considered proportional to the radiance at an effective wavelength. This is due to the following fact: the ratio of two broadband measurements, which are taken under different conditions but with the same instrument (the same spectral response), is equal to the ratio of the same



measurements taken with an instrument which is only sensitive at the effective wavelength,  $\lambda_e$ , calculated as [Kholopov, 1975; Román et al., 2012]:

$$\lambda_e = \frac{\int_{\lambda} \lambda I(\lambda) S(\lambda) d\lambda}{\int_{\lambda} I(\lambda) S(\lambda) d\lambda} \quad (1)$$

where  $I$  is the incoming irradiance to the instrument at the wavelength  $\lambda$ , and  $S$  the spectral response of the instrument channel. In order to obtain the effective wavelength of the SONA sky camera channels in this work, the effective wavelength of each channel has been calculated for a half Moon cycle at every midnight from first to third lunar quarter with  $I$  calculated using the ROLO model. The average ( $\pm$  standard deviation) of the calculated effective wavelengths is  $468.8 \pm 0.3$  nm,  $533.3 \pm 0.3$  nm and  $607.7 \pm 0.2$  nm for blue, green and red channels, respectively. Finally, these effective wavelengths have been rounded to 469 nm, 533 nm and 608 nm, which approximately is within the standard deviation interval. Román et al. [2012] calculated the effective wavelengths for another sky camera under various aerosol conditions, finding standard deviations around 2 nm, which indicated that effective wavelengths of this kind of sky cameras do not vary largely with the real changes on the incoming radiation.

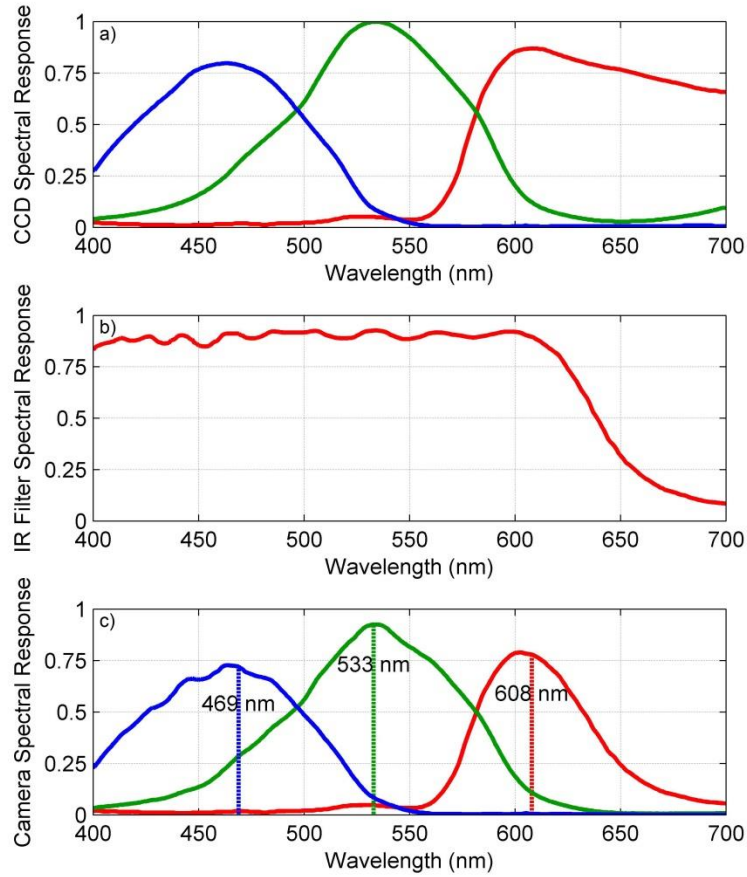
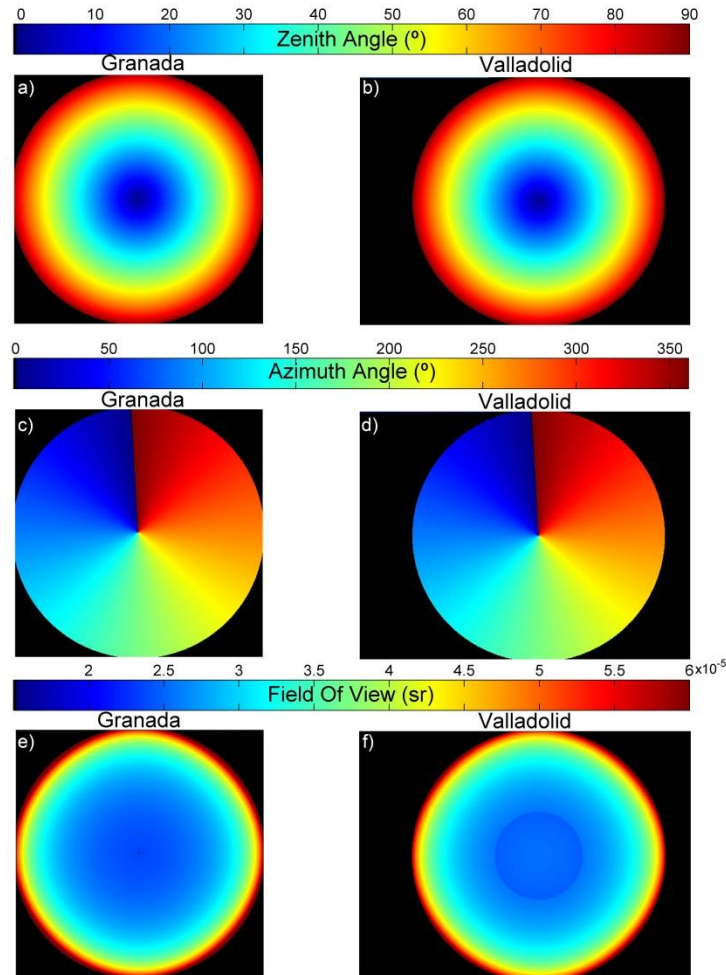


Figure 1: Spectral responses of the three channels (blue, green and red) of the CCD (panel a), of the infrared (IR) cut-off filter (panel b), and of the three channels of the camera (CCD plus infrared cut-off filter; panel c). The effective wavelengths of the camera for lunar applications are marked in panel c.

### 3.1.2- Sky coordinates of each pixel

SONA sky camera position is fixed, thus every pixel measures the same region of the celestial vault. Hence, the zenith and azimuth angles corresponding to all the pixels can be calculated to locate any celestial body in every image (in this work we focus on the position of the Moon and its aureole). The zenith and azimuth matrices have been calculated using a dataset of sky images under cloud-free conditions and visible stars and planets whose celestial coordinates are well-known in these images. The stellar bodies used at Granada have been Arcturus, Jupiter and Vega; while for Valladolid they have been Altair, Arcturus, Jupiter, Saturn, Vega and Venus. The pixel positions of these stellar bodies have been correlated with their sky coordinates, finding a relationship between the zenith and azimuth with pixel position. As a result, Fig. 2

229 presents zenith and azimuth calculated for the cameras at Granada (panels a, c and e)  
 230 and Valladolid (panels b, d and f). The representation of zenith and azimuth angles is  
 231 similar for both cameras. In both cases, a slight shift in the azimuth can be observed in  
 232 the north direction. Moreover, the field of view (FOV) of each pixel has been calculated  
 233 as the solid angle obtained from zenith and azimuth. FOV increases with zenith as can  
 234 be observed in Fig. 2e and 2f. Figure 2 also shows that Valladolid images have a  
 235 resolution of 640x480 pixels whereas resolution is 480x480 pixels for Granada. Zenith  
 236 angles above 80° have been masked in this work since city skylines usually occupy that  
 237 region.



238

239 Figure 2: Zenith (panels a and b), Azimuth (panels c and d) and FOV (panels e and f) viewed by each  
 240 camera pixel at Granada (panels a, c and e) and Valladolid (panels b, d and f). Azimuth is defined from 0°  
 241 (North) to 360° being East 90° and West 270°.

### 3.1.3- Pixel sensitivity

Pixel sensitivity is usually not linear with exposure time in commercial cameras. This is the case for the SONA sky camera. In order to obtain the pixel sensitivity of both cameras, consecutive cloud-free images were taken at different exposure times. Looking at some points of the cloud-free sky, and assuming that the irradiation reaching each pixel must be proportional to the exposure time, the pixel sensitivity function can be obtained by the method explained by Debevec and Malik [1997]. This method uses differently exposed images of the same scene to recover the response function of the imaging process, up to factor of scale, using the assumption of reciprocity. Following this method, the pixel sensitivity of each camera has been calculated under daytime and cloudless conditions for 70 cases distributed in 7 days. These sensitivity values have been averaged for each location, and these averages and their standard deviations are shown in Fig. 3 for both sites and for the three broadband channels. The pixel sensitivity is similar but not equal in the two analyzed cameras. The sensitivity function present similar graphs to those obtained by Debevec and Malik [1997] (see Figs. 2, 4 and 7 of the mentioned paper). The blue channel has the highest sensitivity for low pixel counts, and the saturation effect can be seen at higher pixel counts, where the pixel sensitivity strongly increases. Standard deviation is higher for low pixel counts, which could be associated to fluctuations in the very short exposure times used to reach these pixel counts.

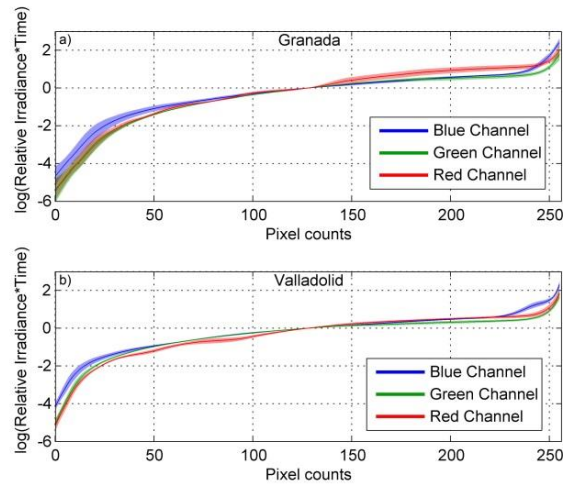


Figure 3: Sensitivity of the camera pixels for each channel as a function of pixel counts for both Granada (panel a) and Valladolid (panel b) cameras. The shadow band around the lines represents the standard deviation.

### 3.1.4- Dark signal

The signal of CCD is not only produced by incoming radiation (photons), but also by thermal energy [Mullikin et al., 1994]; it means that an image taken under dark conditions will show a response different to null, which is called dark image. The response of a dark image usually increases with temperature and with exposure time [Pérez-Ramírez et al., 2008]. These dark images, or dark frames, must be subtracted from an original sky image to remove the thermal noise. Dark signal has been obtained in a different way for both analyzed cameras as detailed below.

The Granada camera was temporally installed in a dark place and covered by an opaque cloth in order to take images in complete dark conditions. Under these dark conditions, the camera recorded dark images at different exposure times and temperature values. The chosen exposure times were the same as the ones that will be shown in Section 3.2.1. The obtained dark images with the same exposure time and temperature have been averaged to reduce the random noise present in single measurements [Urquhart et al., 2015]. These averages have been considered as dark frames (DF). Figure 4 shows the obtained DF (Granada camera) for two different

exposure times and three different temperatures. The signal of the frames is shown upscaled by a factor 4 for better visualization. The dark signal is not equal for all pixels under the same conditions of exposure time and temperature. Temperature has a direct effect on DF with a larger dark signal for higher temperatures. An increase in exposure time also produces higher dark signal values.

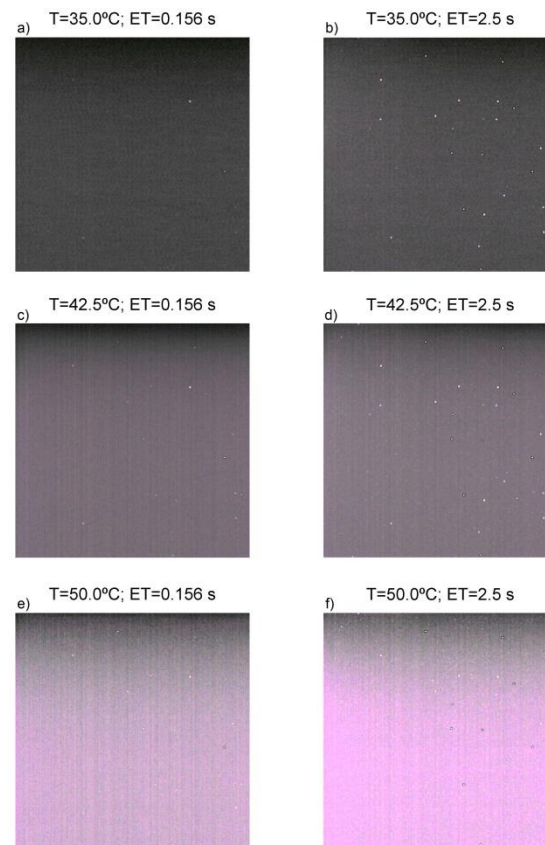


Figure 4: Dark frames obtained with the Granada camera for different temperatures (T) and exposure times (ET). The signal shown is multiplied by 4 in order to be better appreciated.

Figure 5 points out to the same conclusion showing the mode (most frequent value) of all pixels of every dark frame for the channels blue ( $DF_B$ ), green ( $DF_G$ ) and red ( $DF_R$ ) as a function of exposure time and temperature. For low exposure times the dependence of the dark signal on temperature is low but this dark signal presents values higher than zero, indicating the presence of a bias. Dark signal is low while exposure time is below 7 ms, but for higher exposure times it increases especially for high

temperatures. For a given exposure time, the dependence of dark signal on temperature presents an exponential behavior. The logarithm of the dark signal (not shown) presents a negative linear relationship with the inverse of the temperature following the Arrhenius law as previously was observed in a different camera by Widenhorn et al. [2002]. The green channel presents the lower dark signals for high temperatures, while red and blue channels can reach dark signal above 60 digital counts for temperatures near 50°C and high exposure times.

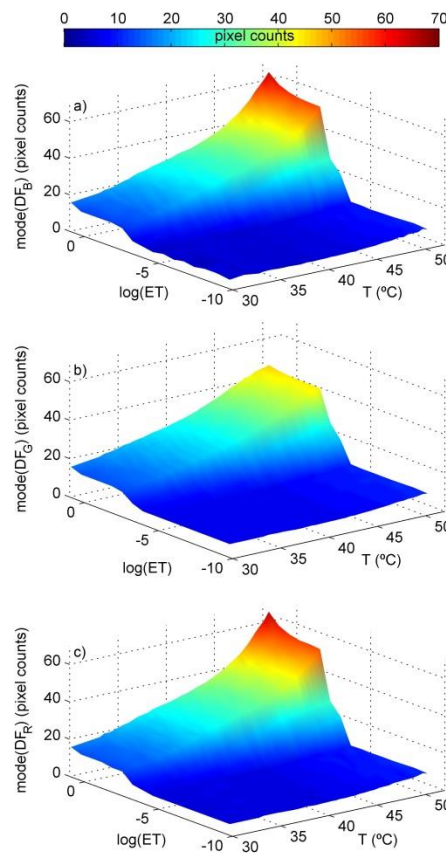


Figure 5: Most frequent value in a dark frame as a function of temperature (T) and logarithm of the exposure time (ET), for the three Granada camera channels.

The dark frame has been corrected for an original sky image and a given exposure time and temperature subtracting the DF (obtained for the same exposure time and temperature) from the non-saturated pixels of the original image. This method has been applied in this work to the Granada camera, but not to the images recorded by the

Valladolid camera since obtaining the dark frames in a dark place was not feasible. In order to obtain a dark frame for the Valladolid images, as a first approach, the dark signal of each channel has been considered the same for all pixels and equal to the average of the signal of various pixels located in a non-illuminated zone, as in Román et al. [2012]. For Valladolid camera the non-illuminated zone has been considered the 33x24 pixel rectangle (proportional to the image size) located at the down-right corner of each image. For each channel (R, G and B) the average of the pixel signals in this zone provides a dark signal, and the dark frame ( $DF_R$ ,  $DF_G$  and  $DF_B$ ) is an image in which all pixels have this same dark signal. Then, for each image taken at Valladolid the calculated DF has been subtracted for the non-saturated pixels.

### **3.1.5- Hot pixels**

Pixels with a very high dark signal are referred as dark current spikes or hot pixels [Widenhorn et al. 2002]. They are generally randomly distributed in a CCD and show up as white, but evenly colored, dots in a dark frame. Hot pixels of the Granada camera can be perfectly appreciated in Fig. 4. The hot pixels of each camera have been determined taking a high exposure image under dark conditions (and low temperature) and considering as hot pixels all the pixels with a signal above 30 digital counts for at least one channel. The obtained hot pixels (not shown) fit well with the hot pixels that can be visually detected in all dark images. Once hot pixels have been identified, they and their neighbors have been masked from all the images.

## **3.2- Retrieval of relative sky radiance**

### **3.2.1- High Dynamic Range imagery**

The CCD provides 256 digital counts per channel, which presents two main problems: some pixels are saturated (in the lunar region in this work), and some pixels



are fully dark; pixels in both situations do not provide useful information about the real radiance. The multi-exposure technique has been used to solve both issues [Debevec and Malik, 1997]. It consists of recording the same image at different exposure times, in order to increase the dynamic range, having images where the brightest parts are not saturated (for the lowest exposure times) and images where the darkest parts are bright enough. Once the images at different exposure times are recorded, a linear High Dynamic Range (HDR) image can be obtained using the pixel sensitivity of the camera (to linearize the output) and applying the method of Debevec and Malik [1997]. As a result, a linear HDR image gives, for each channel and pixel, a signal proportional to the incoming irradiance to the CCD [Stumpf et al., 2014].

In this work, the sky cameras have been configured to record 16 consecutive sky images with exposure times following a doubling sequence. The first image ( $im_1$ ) is taken with an exposure time,  $ET(im_1)$ , then the second image ( $im_2$ ) is taken with an exposure time,  $ET(im_2)$ , equal to  $2 \cdot ET(im_1)$ , then the third ( $im_3$ ) with an exposure time equal to  $2 \cdot ET(im_2) = 2^2 \cdot ET(im_1)$  ..., and finally the last image ( $im_{16}$ ) is taken with a exposure time,  $ET(im_{16}) = 2^{15} \cdot ET(im_1)$ , around 2.5 seconds. The elapsed time obtaining the 16-image dataset is about 30 seconds. The gain (ISO) used for these images has been set to constant at night time, and equal to the one used for obtaining the dark frames (Section 3.1.4). These sequences of 16 images have been taken every five minutes at Granada and Valladolid. As a result, every 5 minutes a linear HDR image has been composed from these 16 images (dark frame corrected) combined with the pixel sensitivity of Fig. 3.

For visualization purposes, a linear tone mapped HDR image would show little detail. To improve visualization, the linear HDR images have been tone mapped following the method described by Reinhard et al. [2002]. This method computes the

key of the HDR image, a measure of the average logarithmic luminance, and then the image is scaled to the desired brightness level. Figure 6 shows three non-HDR images (panels a, b and c) and the corresponding tone mapped images (panels d, e and f). In the non-HDR images the pixels around the Moon are saturated, especially at Granada, while the signal around the Moon can be discerned in the tone mapped images. Also, the masks covering hot pixels can be appreciated in the HDR images.

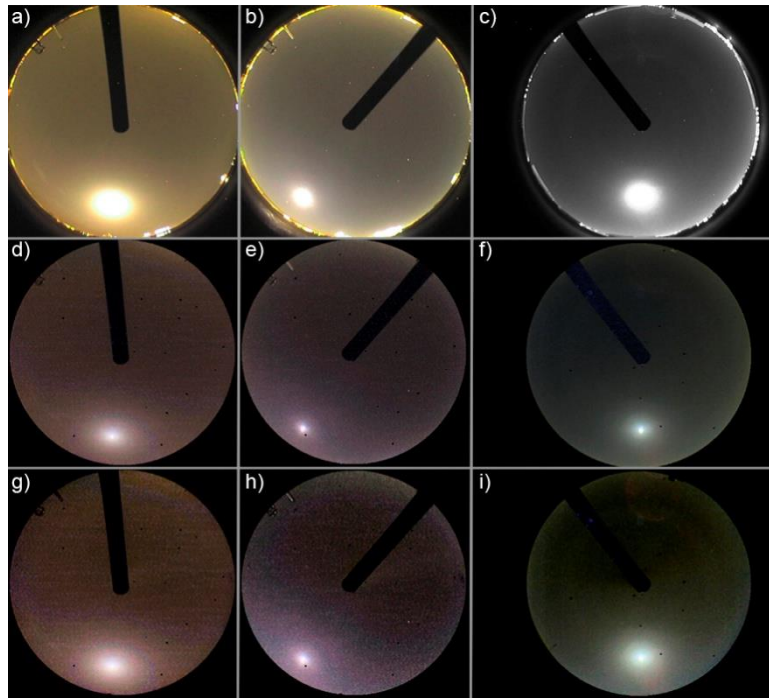


Figure 6: Non-HDR (upper; panels a, b and c) tone mapped sky images before removing background signal (middle; panels d, e and f) and tone mapped sky images with background corrected (bottom; panels g, h and i). Images corresponds to Granada 21<sup>st</sup> July 2016, 00:40UTC (left; panels a, d and g); Granada 20<sup>th</sup> May 2015, 21:25UTC (middle; panels b, e and h); Valladolid 3<sup>rd</sup> August 2015, 02:40UTC (right; panels c, f and i). The non-HDR image at Valladolid was taken under colorless conditions. Pixels with zenith angle above 80° are masked except for non-HDR images.

### 3.2.2- Point spread function

The point spread function (PSF) is the bidimensional signal viewed by a pixel and its neighbors when this pixel is illuminated by a point source. PSF could cause changes on the variation of the signal between pixels near to an illuminated point source (like the Moon). In this work, PSF has been calculated for both cameras using the method explained by Pinilla et al. (1999) which is based on McGillen et al. (1983) and

on Forster and Best (1994). This method basically consists of studying the changes in pixel signal with respect to pixel distance from dark to bright pixels. The first derivative (slope) of the curve of the transition from dark pixels to bright pixels is assumed proportional to the PSF in the selected direction. To this end, diurnal HDR images have been used considering as dark region the pixels containing the camera shadow band, and the bright pixels those containing the blue sky near to the shadow band. For each camera, PSF has been obtained for 6 different images and then averaged. This PSF has been used to correct the HDR images by a deconvolution of PSF on the image using Lucy-Richardson algorithm (Richardson, 1972; Lucy 1974). This correction helps deblurring some parts of the HDR image. However, the night time images show a larger noise, especially near the Moon, which could be associated to a non-perfect PSF characterization. These results suggest that PSF correction could add noise to the HDR images and, therefore, PSF has not been corrected in this work.

### **3.2.3- Background correction**

The nocturnal sky images also recorded part of the city background light (city lamps, buildings and others). As a consequence, the sky is not fully dark even without Moon. The lunar aureole viewed by the camera can be contaminated by these lights, hence, in order to detect the Moon aureole, the city lights need to be characterized and removed for the original HDR image. With this aim, a data base of background images (BG) has been constructed from images taken under cloud-free conditions and with both Moon Zenith Angle (MZA) and Solar Zenith Angle (SZA) above 100°. In these conditions, we guarantee that the images are not contaminated by the Moon nor the Sun light and neither the clouds. Note that these BG images have been taken at low illumination and they usually are quite noisy. To partially correct for this effect, all the BG images have been smoothed by an averaging filter of 5x5 pixels.

As a first guess, we could assume that the signal of background images depends on the aerosol load, since aerosols can scatter part of the city lights back to the camera. The data base of BG images has been analyzed and correlated to the closest AOD value measurement (note that there are no simultaneous measurements of AOD since BG images are taken under skies without the Sun and Moon). The maximum gap allowed between BG images and AOD measurements has been 3 hours for Granada and 4 hours for Valladolid due to the lower number of images available in the latter. AODs at 440, 500 and 675 nm have been assigned to the blue, green and red channels of the camera, respectively. The determination coefficient ( $r^2$ ) between the pixel signal of each channel and its AOD value has been calculated using the chosen BG images for both cameras (151 images for Granada and 61 for Valladolid). Figure 7 shows the obtained determination coefficient for every pixel, channel and camera, pointing out that red channel presents the best correlation between the background signal and the AOD. However, the correlation is not high, since the  $r^2$  values at Granada are usually below than 0.5, 0.4 and 0.2 for the red, green and blue channels, respectively. The correlation at Valladolid is lower, being  $r^2$  below 0.4 in most of pixels for all channels, but this behavior could be explained by the short AOD range used for the calculation of  $r^2$ : AOD at 440 nm ranges from 0.03 to 0.13 and AOD at 675 nm from 0.01 to 0.06. However, for Granada camera the AOD intervals have been larger, ranging from 0.03 to 0.35 (AOD at 440 nm) and from 0.01 to 0.33 (AOD at 675 nm). These results indicate that background light does not present a clear dependence on AOD and, therefore, BG images have been considered as independent on aerosol load.

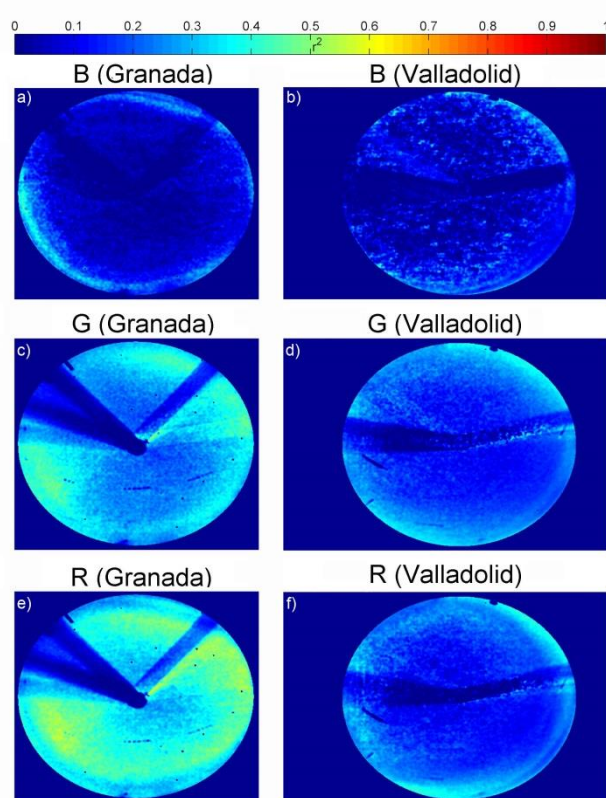


Figure 7: Determination coefficient ( $r^2$ ) between the background pixel signal and the AOD assumed at each channel. These values are shown for each channel at Granada (left; a-c-e) and Valladolid (right; b-d-f). Pixels with zenith angle above  $80^\circ$  are masked.

Assuming that the background light from the city is constant, an averaged BG image (ABG) has been calculated for each location in order to remove the noise and fluctuations of single BG images. To this end, a set of BG images under clean (low aerosol load) conditions have been chosen, trying to obtain similar conditions for all images despite of the observed low correlation between BG and AOD. The selected night BG images also satisfy that previous and next diurnal AOD at 440 nm measurements were below 0.1. A total of 182 and 156 BG images for Granada and Valladolid, respectively, have been chosen by these criteria, and then they have been averaged. As a result, the ABG has been obtained and is shown in Fig. 8 for Granada and Valladolid, being representative of the background light of each location. ABG images of Fig. 8 include a spot in the sky zenith which is not representative of the

background light but it is caused by the shadow band, which always block this position. This artefact does not affect results in this work since the Moon never reaches that position.

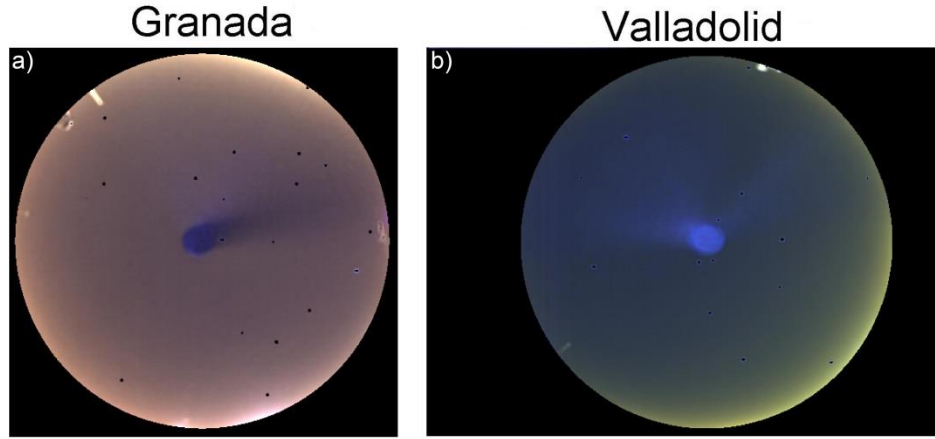


Figure 8: Averaged background HDR images obtained at Granada (panel a) and Valladolid (panel b). Images are not tone mapped and pixels with zenith angle above  $80^\circ$  are masked.

Finally, all obtained HDR images have been corrected subtracting the corresponding ABG of Fig. 8. Figures 6g, 6h and 6i present the tone maps of three HDR images after the background correction, showing significant differences against the non-corrected images.

### 3.2.4- Normalized Lunar Almucantar extraction

Once the background light is removed from the HDR image, the relative radiance at the lunar aureole can be obtained. First, every pixel signal has been divided by its FOV, in order to transform the recorded relative irradiance in the CCD to relative sky radiance (RSR). Several points of the lunar almucantar (points with same zenith angle of the Moon but different azimuths) have been selected and located in the image, and the signal in the pixels within  $\pm 0.5^\circ$  azimuth and  $\pm 0.5^\circ$  zenith have been averaged for each channel. The points selected range from azimuth  $3^\circ$  to  $20^\circ$  azimuth ( $1^\circ$  steps) away from the Moon. The first azimuth angle has been chosen at  $3^\circ$  in agreement with

the first angle of the almucantar measurements sequence used in the AERONET photometers [Holben et al., 2006]; the last azimuth of 20° has been manually selected since it was observed that beyond 20° the camera signal does not significantly change. In addition, pixel signals which are below the double of the corresponding ABG signal have been discarded even if the azimuth is below 20°. This criterion has excluded several RSR values for very low AOD or low Moon irradiance (at least between the third and first Moon quarters); in both cases the scattered light in the lunar aureole region is low.

Once the points of almucantar are selected (3° to 20° and -3° to -20° with at least the double of background signal), both branches of the almucantar have been averaged assuming the sky radiance is symmetric. The number of averaged pixels for each almucantar point (considering its azimuth and its symmetric azimuth) depends on zenith angle because of the lens distortion (see Fig. 2); this number is around 8 pixels for zenith equal to 20°, increasing up to 16 pixels for zenith values of 60° and going down to about 12 pixels for zenith equal to 80°. Finally, for each channel, the obtained signals have been normalized by the sum of all of them, giving as result the normalized camera radiance (NCR); the sum of the normalized camera radiances must be 1 for each channel. Then, the normalized camera radiance at a given  $\lambda$ -wavelength and a  $\varphi_i$ -angle has been calculated as:

$$NCR_{\lambda, \varphi_i} = \frac{RSR_{\lambda, \varphi_i}}{\sum_{j=1}^N RSR_{\lambda, \varphi_j}} \quad (2)$$

where N is the number of points used to extract the almucantar.

Figure 9a shows the normalized lunar almucantar radiance obtained using this method for the HDR image on Fig. 6g; the straight lines are the averaged values from both branches, and the azimuth value of the Moon is considered to be 180°.

#### **4- GRASP code**

GRASP (Generalized Retrieval of Aerosol and Surface Properties) is a highly accurate algorithm for the retrieval of optical and microphysical aerosol properties and optical surface properties [Dubovik et al., 2014]. GRASP stands out by its versatility (it can be run with a large variety of input variables) and its flexibility (it has the capacity to incorporate and exchange different methods, modules and libraries). This code has been used by other authors with lidar systems, photometers and satellites [Lopatin et al., 2013; Kokhanovsky et al., 2015; Bovchaliuk et al., 2016; Fedarenka et al., 2016; Benavent-Oltra et al., 2017], but not with sky cameras until now. Another important advantage of GRASP is that it is open-source and free (available at [www.grasp-open.com](http://www.grasp-open.com)).

##### **4.1- Forward model**

GRASP has two main independent modules. One of them is the forward model, which allows the simulation of various atmospheric observations [Dubovik et al., 2014]. In this work, this module has been used to simulate the lunar normalized radiance at the same points that were obtained with the camera. Aerosol properties obtained from AERONET have been used as inputs to make these simulations of normalized radiance on the lunar almucantar for the three camera effective wavelengths. For a given night, the nearest AERONET aerosol inversion of the previous afternoon or the next morning



has been chosen. The AERONET aerosol properties used from this inversion have been: 22-bin volume size distribution (logarithmically spaced), real and imaginary refractive indices at four wavelengths, and sphere fraction. In order to obtain the radiance at the camera wavelengths the refractive indices at these wavelengths is needed; therefore the refractive indices at 469, 533 and 608 nm have been calculated using a linear interpolation of the AERONET available values. All these aerosol properties and, in addition, the MZA have been introduced into GRASP forward model. The output of the model has given the normalized radiance in the lunar almucantar at 469 nm, 533 nm and 608 nm.

#### **4.2- Aerosol retrieval**

The main module of GRASP is the numerical inversion, which includes general mathematical operations not related to the particular physical nature of the inverted data [Dubovik et al., 2014]. This module, in combination with the forward module, can retrieve aerosol properties from a data set of atmospheric measurements. GRASP is configured to process absolute radiances but also normalized radiances. The inverted data set in this work, used as input in GRASP, have been six values of AOD (440, 500, 675, 870, 1020, and 1640 nm) from CE318-T photometer and the normalized radiance from the camera at 469 nm, 533 nm and 608 nm at 36 points per wavelength (lunar almucantar points from 183° to 200° every 1°). A bilognormal size distribution has been selected in order to represent the retrieved size distribution (instead of the 22-bin representation used in AERONET), and different smoothness and “a priori” constraints on the aerosol size distribution have been applied [Dubovik et al., 2014]. Aerosol refractive indices, both real (RRI) and imaginary (IRI), have been assumed as constant (non spectral variation); this assumption has been done due to the lack of information

regarding the diurnal retrievals which consider that refractive indices can vary with wavelength.

As a result, for each HDR image and 6-AOD dataset, the following parameters have been obtained: bilognormal size distribution, real and imaginary refractive indices, single scattering albedo (SSA) at the same wavelengths than input values, and sphere fraction. The retrieved bilognormal size distribution is described by six independent parameters [Torres et al., 2016]: volume concentration of the fine ( $C_f$ ) and coarse mode ( $C_c$ ); volume median radius of the fine ( $r_f$ ) and coarse mode ( $r_c$ ), and geometric standard deviation for both modes:  $\sigma_f$  (fine) and  $\sigma_c$  (coarse). This geometric standard deviation is related to the width of the size distribution centered in the median radius.

## **5- Results**

### **5.1- Camera radiances versus simulations**

As described in the introduction, the first step will be the validation of the normalized radiances obtained with the sky camera. For this purpose, the lunar almucantars obtained from the camera and their equivalent simulated with the GRASP forward model have been compared on different nights.

#### **5.1.1- Individual case**

A desert dust plume was detected at Granada during the evening of 20<sup>th</sup> July 2016. The ceilometer signal (not shown) indicated that it arrived in Granada at around 15:00 UTC. The AERONET values of Table 1 point out the presence of desert dust after 15:00 UTC: Angström Exponent at 17:55 UTC was 0.2, indicating coarse particle predominance with a strong AOD at 440 nm of 0.98. The AOD along the night (not

shown) did not present significant changes and the AERONET retrieval at the next morning (not shown) is similar to the one shown in Table 1. Therefore, the aerosol characteristics did not present relevant variations along the night from 20<sup>th</sup> to 21<sup>st</sup> July 2016. That night the Moon Phase Angle (MPA) was 13° at midnight (one day after full Moon), therefore with a large Moon irradiance associated. The normalized radiance at lunar almucantar geometry has been obtained from the sky camera at various night times. The radiance has also been simulated at the same times using as input the AERONET aerosol optical properties obtained the afternoon of 20<sup>th</sup> July at 17:55 UTC (Table 1) and the size distribution (not shown in Table 1).

Table 1: Retrieved aerosol optical properties from AERONET sunphotometer (level 1.5) near to the previous sunset or the following sunrise for eight nights.

Properties	Wavelength (nm)	29 May 2015 07:45 UTC	3 Aug 2015 06:43 UTC	21 Feb 2016 15:35 UTC	19 May 2016 06:27 UTC	20 May 2016 18:03 UTC	24 May 2016 09:24 UTC	20 July 2016 17:55 UTC	24 July 2016 06:37 UTC
Place	-	Valladolid	Valladolid	Valladolid	Granada	Granada	Granada	Granada	Granada
Photometer ID		#788	#788	#383	#918	#918	#918	#918	#918
Real RI	440	1.39	1.44	1.50	1.35	1.45	1.45	1.42	1.33
	675	1.41	1.44	1.48	1.36	1.44	1.45	1.44	1.34
	870	1.42	1.44	1.47	1.37	1.45	1.45	1.44	1.37
	1020	1.42	1.43	1.46	1.38	1.43	1.44	1.41	1.37
Imaginary RI	440	0.0035	0.0073	0.0035	0.0106	0.0093	0.0053	0.0038	0.0055
	675	0.0030	0.0031	0.0008	0.0082	0.0073	0.0017	0.0010	0.0049
	870	0.0029	0.0029	0.0005	0.0085	0.0073	0.0014	0.0008	0.0053
	1020	0.0029	0.0031	0.0005	0.0083	0.0071	0.0013	0.0007	0.0054
AOD	440	0.20	0.27	1.84	0.21	0.23	0.36	0.98	0.22
	675	0.09	0.20	1.82	0.10	0.11	0.31	0.93	0.11
	870	0.07	0.18	1.75	0.07	0.08	0.30	0.89	0.09
	1020	0.05	0.17	1.70	0.05	0.06	0.29	0.85	0.07
Angström Exponent	440-870	1.6	0.6	0.1	1.7	1.5	0.3	0.2	1.4
Sphere fraction (%)	-	97	3	0	97	98	1	0	94

Figure 9a shows the obtained camera almucantar for the image of Fig. 6g for Granada on 20<sup>th</sup> July 2016 at 00:40 UTC. This almucantar is similar to the simulated one (Fig. 9b), both showing the highest radiances near the Moon at 469 nm, followed by 533 nm. Finally for this case, the ratio between the camera and the simulated

normalized radiances has been represented in Fig. 9c as a function of azimuth for different HDR images taken that night. This ratio presents values near to 1 for all wavelengths, except for the highest azimuth values where the ratio fluctuates especially for 469 nm. These results indicate a good agreement between measurements and simulations for this case.

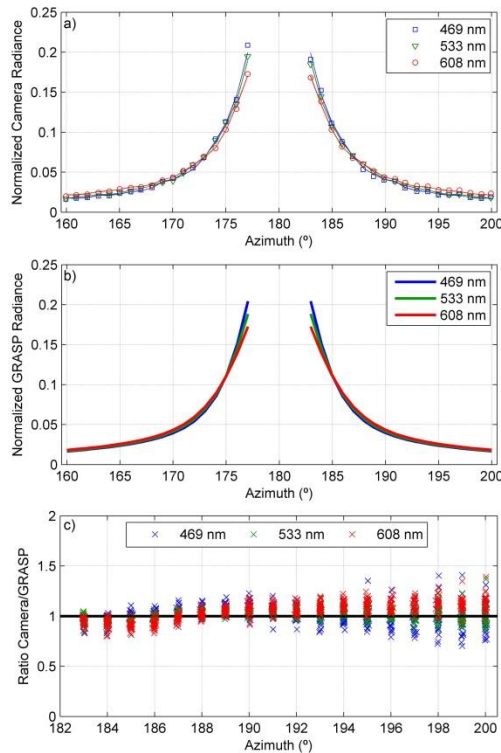


Figure 9: Normalized lunar almucantar radiances from camera (panel a) and simulated ones by GRASP (panel b) for Granada 21<sup>st</sup> July 2016, 00:40UTC. Panel c shows the ratio of normalized camera radiance to normalized GRASP radiance along the night 20<sup>th</sup>-21<sup>st</sup> May 2016 as a function of azimuth.

### 5.1.2- Statistical analysis

In addition to the analyzed case, seven other nights have been added to the dataset for comparison, with a total of 8 nights (4 cases with fine aerosol predominance and 4 coarse aerosol cases), 5 at Granada and 3 at Valladolid. The normalized radiances have been simulated for the eight nights as in the previous case using the parameters of the AERONET retrievals (corresponding to the afternoon before or to the morning after) shown in Table 1. Clean cases (low aerosol load) have not been considered due to the

uncertainties in the aerosol parameters under low aerosol load. In fact, the aerosol parameters retrieved by AERONET present quality assurance only when the AOD at 440 nm is higher than 0.4 [Holben et al., 2006]; however, due to the lack of coincident cases with high AOD values and camera measurements under stable and constant aerosol conditions along a full night, AERONET data used were retrieved with AOD at 440 nm higher than 0.2, with only two cases of AOD at 440 nm above 0.4 (related to coarse particle events).

Figure 10 shows the scatter plots (one per wavelength) of normalized camera radiance against simulated radiances for the eight nights. The aerosol type of each night is also available at Table 2. The normalized camera radiances show a high correlation with the simulated one for all nights, but normalized radiance at 469 nm presents the largest deviation. Some of the cases present high normalized radiances due to a lack in the number of data in the lunar almucantar caused by the criteria explained in Section 3.2.4: Moon intensity likely too low (near quarters). If the number of points of lunar almucantar decreases, the normalized radiance values increase.

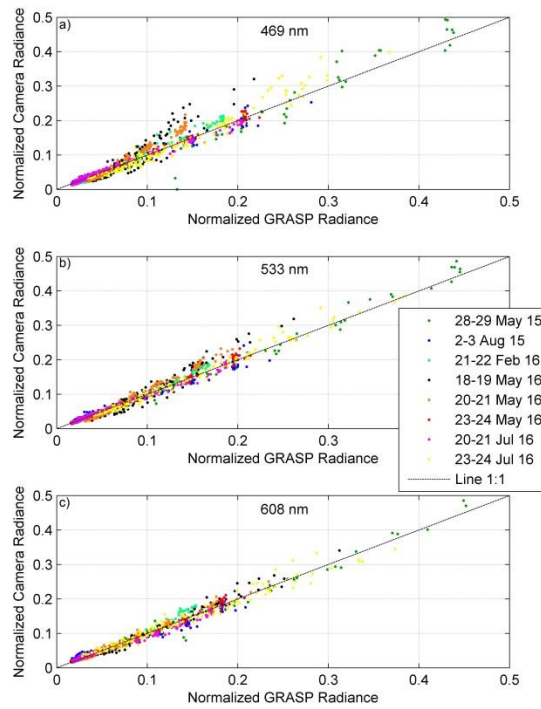


Figure 10: Normalized radiance from camera as a function of simulated by GRASP for 8 different nights at 469 nm (panel a), 533 nm (panel b) and 608 nm (panel c).

Table 2 shows the slope, y-intercept and determination coefficient of the least squares fit between camera and simulated radiances. A large correlation is observed, with  $r^2$  values above 0.90 for all cases, the fine aerosol cases presenting the lowest correlation. From all the cases, the values at 469 nm have the lowest correlation but the overall  $r^2$  is still high at 0.96. The slope of the fit frequently indicates that the values from the camera overestimate the simulations for shorter wavelengths. The y-intercept values usually decrease in absolute value with wavelength, being farther from zero for the fine aerosol cases, especially at 469 and 533 nm. When all the analyzed nights are considered together, the fit slope shows that camera radiance overestimates around 6% and 3% the simulations at 469 and 533 nm, respectively, being the slope equal to 1.00 for 608 nm. These results point out that normalized camera radiance is in good agreement with the simulated radiance, especially at 608 nm.

Table 2: Statistical parameters of the scatter plots of normalized camera radiance against simulated one for three wavelengths and different cases. N is the number of available data pairs for each wavelength.

Case (Type)	Wavelength (nm)											
	469				533				608			
	N	Slope	y-intercept	r <sup>2</sup>	N	Slope	y-intercept	r <sup>2</sup>	N	Slope	y-intercept	r <sup>2</sup>
Valladolid 28-29 May 2015 (Fine)	43	1.16	-0.0490	0.93	36	1.03	-0.0100	0.99	42	1.03	-0.0082	0.99
Valladolid 2-3 August 2015 (Coarse)	275	0.94	0.0034	0.98	281	0.90	0.0054	0.98	285	0.88	0.0070	0.98
Valladolid 21-22 Feb 2016 (Coarse)	522	1.12	-0.0064	0.99	522	1.05	-0.0028	0.99	522	1.09	-0.0049	0.98
Granada 18-19 May 2016 (Fine)	275	1.51	-0.0349	0.90	232	1.29	-0.0236	0.96	228	1.10	-0.0086	0.98
Granada 20-21 May 2016 (Fine)	502	1.48	-0.0268	0.99	464	1.29	-0.0176	0.99	462	1.06	-0.0035	0.99
Granada 23-24 May 2016 (Coarse)	299	1.03	-0.0016	1.00	294	1.02	-0.0009	0.99	297	0.99	-0.0005	0.99
Granada 20-21 July 2016 (Coarse)	504	0.95	0.0025	0.99	504	0.97	0.0019	1.00	504	0.90	0.0057	0.99
Granada 23-24 July 2016 (Fine)	154	1.18	-0.0232	0.97	141	1.05	-0.0075	0.99	158	0.96	0.0046	0.97
All	2574	1.06	-0.0042	0.96	2474	1.03	-0.0020	0.99	2498	1.00	-0.0001	0.99

617

618 For an in-depth analysis, the relative differences ( $\Delta NR$ ) between the camera and  
619 simulations have been calculated for each night, image and channel as:

$$620 \quad \Delta NR(\%) = 100\% \frac{NCR - NGR}{NGR} \quad (3)$$

621 where NCR is the normalized radiance of the camera and NGR (normalized GRASP  
622 radiance) the simulated one.  $\Delta NR$  has been calculated using all available data and its  
623 distribution is shown for different azimuth angle intervals in Fig. 11. The green channel  
624 presents the lowest changes on bias (mean of  $\Delta NR$ ) being near zero for all azimuth  
625 values, while for high azimuth values the camera measurements over/under-estimates  
626 the simulations near the Moon at blue/red channel. These bias values are also shown in  
627 Table 3, ranging from -3.2% (469 nm) to 1.5% (608 nm) when all azimuth values are

considered. The standard deviation ( $\sigma$ ) increases with azimuth and the highest values are found for 469 nm. The standard deviation can be assumed as the uncertainty if the  $\Delta NR$  distribution is Gaussian, which implies that the percentage of  $\Delta NR$  data (absolute value) lower than standard deviation ( $P < \sigma$ ) must be about 68%, and the percentage of  $\Delta NR$  data (absolute value) lower than two standard deviations ( $P < 2\sigma$ ) must be around 95% [Román et al., 2014a].

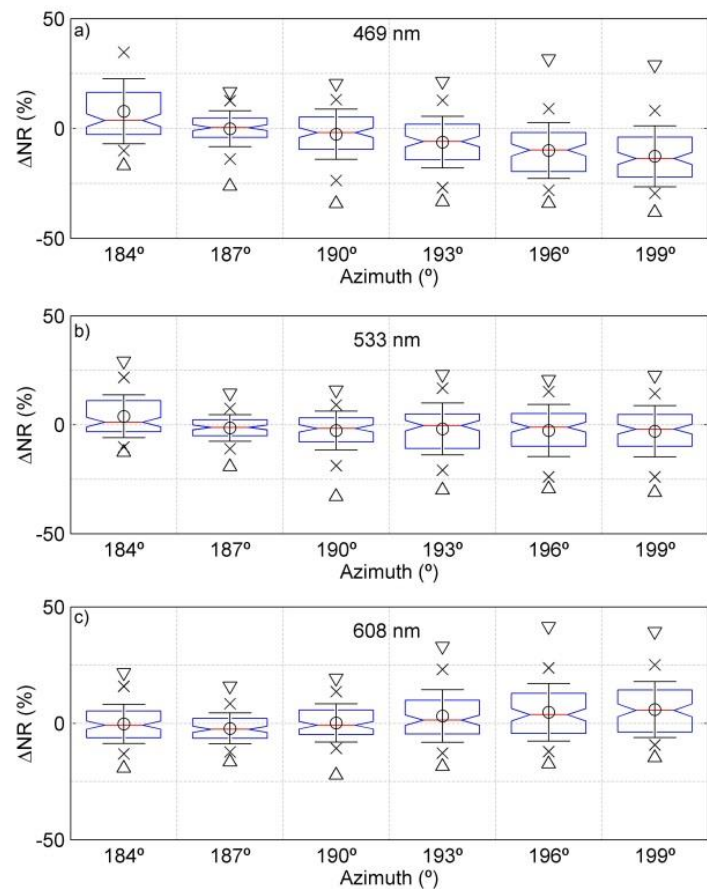


Figure 11: Box plots for the relative distribution of  $\Delta NR$  at 469 nm (panel a), 533 nm (panel b) and 608 nm (panel c) for different azimuth intervals. The box limits are the 25 and 75 percentiles, the error bar is the standard deviation, the circle is the mean, the red line inside the box is the median, the crosses are the 5 and 95 percentiles, and the triangles are the 1 and 99 percentiles.

Table 3 presents the values of  $P < \sigma$  and  $P < 2\sigma$ , which are close to 68% and 95% for all cases, especially for 533 and 608 nm, hence the standard deviation can be considered as the uncertainty of the normalized camera radiance. Then, uncertainty for azimuth intervals from 182.5° to 191.5° falls within 8%-15%, 6%-10% and 7%-8% for 469 nm,



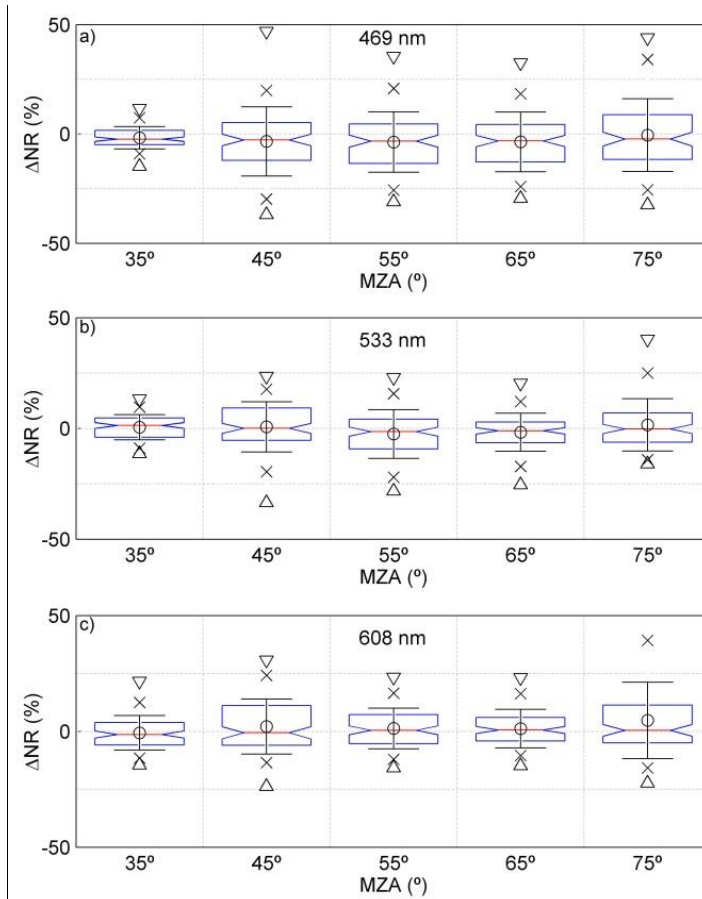
573 nm and 608 nm, respectively. The obtained uncertainty considering all data at each channel (~2500 data) is 14%, 10% and 10% for 469 nm, 533 nm and 608 nm, respectively. In general the fit between measurements and simulations is similar for the green and red channels and slightly worse for the blue channel.

Table 3: Statistical estimators of  $\Delta NR$  for different azimuth intervals and three wavelengths. N is the number of data used;  $\sigma$  is the standard deviation, RMSE is the root mean square difference between camera and simulated radiances;  $P < \sigma$  is the percentage of  $\Delta NR$  values inside the interval  $(-\sigma, \sigma)$ ; and  $P < 2\sigma$  is the percentage of  $\Delta NR$  values inside the interval  $(-\sigma, 2\sigma)$ .

	Wavelength (nm)	Azimuth interval (°)						
		182.5- 185.5	185.5- 188.5	188.5- 191.5	191.5- 194.5	194.5- 197.5	197.5- 200.5	182.5- 200.5
N	469	505	475	438	399	389	368	2574
	533	501	468	429	392	358	326	2474
	608	499	475	437	390	366	331	2498
Mean (%)	469	7.85	-0.08	-2.61	-6.23	-10.02	-12.67	-3.21
	533	3.87	-1.47	-2.63	-1.92	-2.64	-2.94	-1.02
	608	-0.29	-2.19	0.19	3.15	4.73	5.92	1.53
Median (%)	469	3.73	0.42	-1.83	-5.85	-9.78	-13.64	-3.06
	533	1.26	-1.20	-1.66	-0.35	-1.08	-2.00	-0.60
	608	-0.73	-2.54	-0.81	1.39	3.70	5.60	0.17
$\sigma$ (%)	469	14.84	8.15	11.40	11.73	12.71	13.91	14.06
	533	9.83	6.07	8.87	11.92	11.98	11.72	10.38
	608	8.42	6.61	8.23	11.32	12.39	12.00	10.19
$P < \sigma$ (%)	469	70.30	74.95	73.74	59.90	52.19	47.83	71.10
	533	66.47	71.58	73.89	67.60	66.48	69.94	72.39
	608	69.14	69.05	72.54	71.28	68.85	66.77	73.66
$P < 2\sigma$ (%)	469	90.69	94.53	93.84	91.23	89.20	91.58	94.76
	533	93.01	94.44	93.47	96.43	94.69	94.17	93.98
	608	95.79	94.97	94.97	94.10	96.17	93.05	95.56

The obtained results have been calculated using the eight nights simulated with the properties of Table 1. However, only two retrievals of Table 1 satisfy the criteria of quality assurance of AERONET at 440 nm; then if the same analysis is done for all azimuth values with only these two cases, the uncertainty of the normalized camera radiance decreases to 11%, 6% and 9% for 469 nm, 533 nm and 608 nm, respectively. These uncertainty values range between 5%-14% (469 nm), 4%-7% (533 nm) and 6%-9% (608 nm) for the different azimuth intervals.

659 The  $\Delta NR$  distribution has been represented for different MZA intervals in Fig.  
 660 12. The best agreement between camera and simulations appears at MZA values from  
 661  $30^\circ$  to  $40^\circ$ , as percentile 5 and 95 indicate for all wavelengths, but this behavior is not  
 662 significant since only one of the eight nights analyzed reached these low MZA values.  
 663 The mean, median and standard deviation values do not show a clear dependence on  
 664 MZA. The values of  $P < \sigma$  and  $P < 2\sigma$  (Table 4) show that the standard deviation can be  
 665 considered the uncertainty of the normalized camera radiances, and the lowest values of  
 666 this uncertainty are for  $30^\circ$ - $40^\circ$  interval (5%-7%), followed by  $60^\circ$ - $70^\circ$  interval (8%-  
 667 14%). The worse agreement appears for the largest MZA values, which could be due to  
 668 the stronger background light at these angles.



669  
 670 Figure 12: Box plots for the relative distribution of  $\Delta NR$  at 469 nm (panel a), 533 nm (panel b) and 608  
 671 nm (panel c) for different MZA intervals. The box limits are the 25 and 75 percentiles, the error bar is the  
 672 standard deviation, the circle is the mean, the red line inside the box is the median, the crosses are the 5  
 673 and 95 percentiles, and the triangles are the 1 and 99 percentiles.

Table 4: Statistical estimators of  $\Delta NR$  for different MZA intervals and three wavelengths. N is the number of data used;  $\sigma$  is the standard deviation, RMSE is the root mean square difference between camera and simulated radiances;  $P < \sigma$  is the percentage of  $\Delta NR$  values inside the interval  $(-\sigma, \sigma)$ ; and  $P < 2\sigma$  is the percentage of  $\Delta NR$  values inside the interval  $(-2\sigma, 2\sigma)$ .

	Wavelength (nm)	MZA interval (°)				
		30-40	40-50	50-60	60-70	70-80
N	469	216	590	970	596	202
	533	216	562	944	561	191
	608	216	578	962	554	188
Mean (%)	469	-1.75	-3.42	-3.70	-3.64	-0.53
	533	0.51	0.71	-2.51	-1.74	1.60
	608	-0.64	2.08	1.26	1.18	4.72
Median (%)	469	-2.37	-2.75	-3.30	-3.21	-2.30
	533	1.36	0.07	-1.42	-1.06	-0.21
	608	-1.37	-0.61	0.50	0.62	0.46
$\sigma$ (%)	469	5.09	15.85	13.84	13.70	16.64
	533	5.70	11.32	10.97	8.62	11.78
	608	7.46	11.88	8.76	8.28	16.48
$P < \sigma$ (%)	469	67.59	72.03	67.32	68.79	69.80
	533	63.43	70.28	69.70	73.44	75.39
	608	73.15	68.86	67.88	72.74	81.91
$P < 2\sigma$ (%)	469	94.91	93.90	94.95	96.48	93.07
	533	97.69	94.66	93.64	93.23	94.76
	608	95.37	93.60	96.26	94.77	93.09

## 5.2- Retrieval of aerosol properties

A desert dust event arrived at Valladolid the night from 2<sup>nd</sup> to 3<sup>rd</sup> August 2015. Figure 13 shows the AOD and Angström Exponent on both days during the day-night period. The aerosol load during 2<sup>nd</sup> August was low, with an AOD at 440 nm close to 0.1 during all day and Angström Exponent about 1.5, indicating fine mode predominance. However, at the beginning of the next day, the AOD at 440 nm was about three times higher and the Angström Exponent was 0.5 (indicating coarse particle predominance). The night time measurements of the CE318-T photometer show that about 22:30 UTC the AOD started to increase while Angström Exponent began to

decrease; indicating the dust plume outbreak. Ceilometer profiles and back-trajectories (not shown) confirm the Saharan dust outbreak that night.

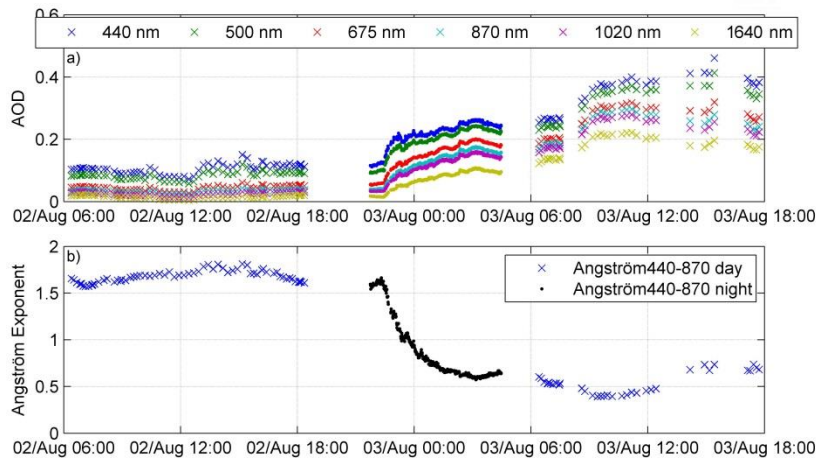


Figure 13: Spectral AOD (panel a) and Angström Exponent (panel b) at day and night from 2<sup>nd</sup> to 3<sup>rd</sup> August 2015 at Valladolid. Crosses and points represent nocturnal and diurnal data, respectively.

The normalized radiance obtained from the SONA camera has been calculated for that night and it has been used as input in GRASP together with the 6 spectral AOD measurements derived from direct lunar observations, as commented in Section 4.2. The GRASP retrievals for that night have been run every 15 minutes, but there is a lack of data around midnight when the camera was not operative. One of the HDR images used in this analysis is the one shown in Fig. 6i. Figure 14 shows the retrieved real (panel a) and imaginary refractive (panel b) indices, sphere fraction (panel c) and SSA values (panel d). The previous and next daytime AERONET values are also included in the graphs. Real part of refractive index presented values around 1.40 and 1.49 and with an error bar that fits with the diurnal AERONET retrievals. The imaginary part of the refractive index shows more fluctuations along the night and with a large error bar; the most IRI values are low once the dust aerosol appeared, as the AERONET value of the next morning. Sphere fraction also shows the dust intrusion in the night since at the beginning of the night the aerosols were mainly spherical but they progressively changed to predominance of non-spherical particles, i.e. desert dust. These changes can

be also appreciated in the wavelength dependence of SSA, since at the beginning of the night the SSA was higher for shorter wavelengths but this fact changed with the dust intrusion, which typically presents lower SSA values for shorter wavelengths.

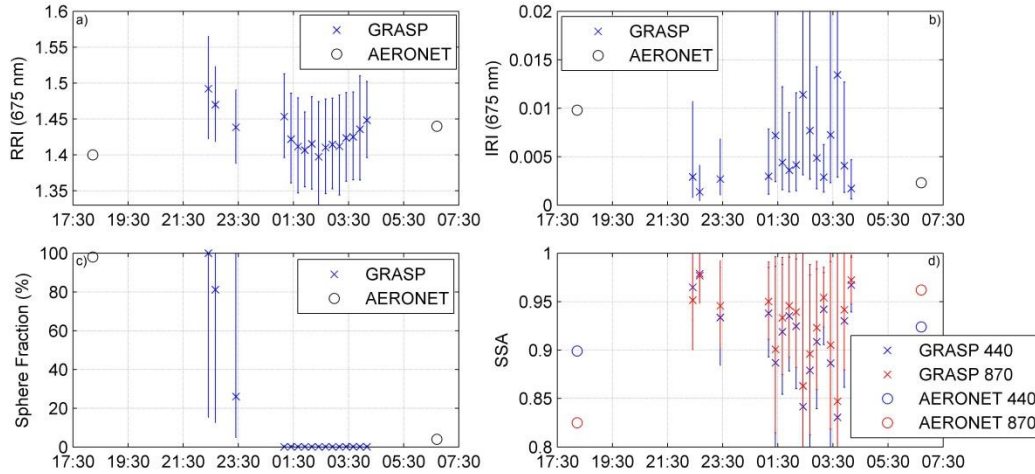


Figure 14: Evolution of the real (panel a) and imaginary (panel b) refractive indices, sphere fraction (panel c) and SSA (panel d) at Valladolid from 2<sup>nd</sup> to 3<sup>rd</sup> August 2015. Diurnal values retrieved by AERONET are represented as circles, while nocturnal values retrieved by GRASP, using normalized camera radiances and nocturnal AOD, are represented by crosses with their error bars.

Regarding the volume size distribution, Figure 15 shows the volume median radius (panels a and b), the geometric standard deviation (panels c and d) and the volume concentration (panels e and f) for both fine and coarse modes. Diurnal retrieved values from AERONET are also included. Regarding the fine mode, the properties do not present strong changes along the night, being similar the retrieved (night time) properties and the AERONET ones. The  $r_c$  values decreased along the night being centered around  $2 \mu\text{m}$  after midnight; this variation is in agreement with the AERONET data. Volume concentration of the coarse mode,  $V_c$ , is also in agreement with the AERONET values since it presented values around  $0.03 \mu\text{m}^3/\mu\text{m}^2$  at the beginning of the night and this concentration raised up to around  $0.1 \mu\text{m}^3/\mu\text{m}^2$  at the end of the night. The geometric standard deviation values of coarse mode  $\sigma_c$  obtained by GRASP are higher than the nearest AERONET product, which indicates that the coarse mode of the size distribution was wider at night.

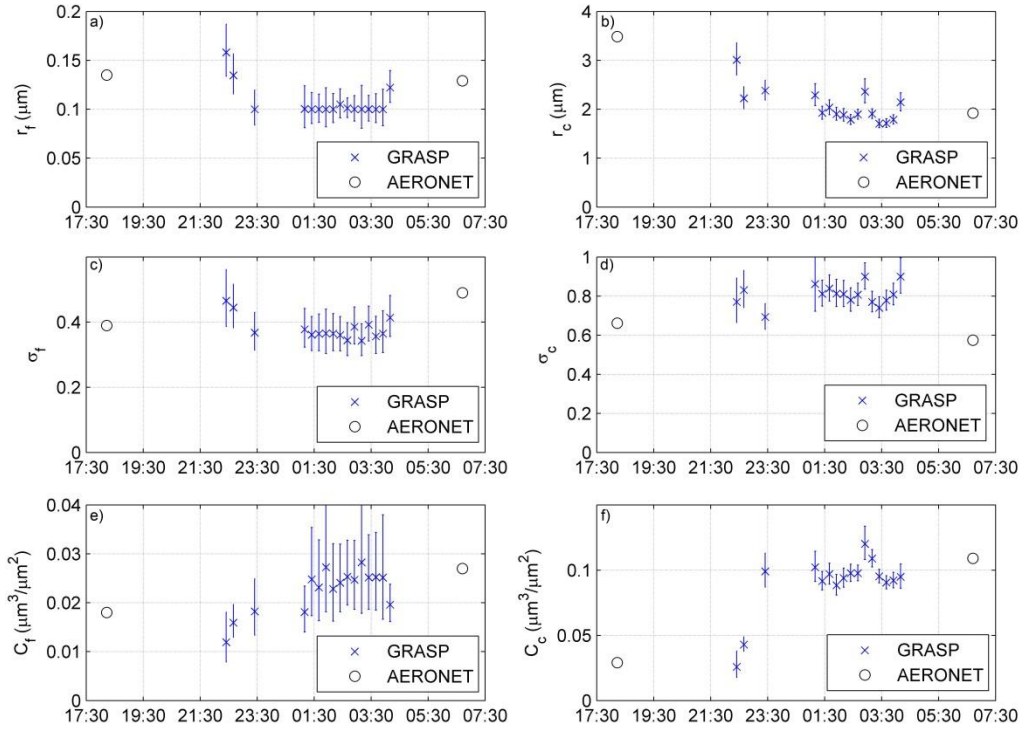


Figure 15: Parameters of the fine (panels a, c and e) and coarse (panels b, d and f) aerosol size distributions from AERONET (black circles) and from GRASP retrieval using normalized camera radiances and nocturnal AOD (blue crosses with error bars) at Valladolid from 2<sup>nd</sup> to 3<sup>rd</sup> August 2015.

## 6- Conclusions

Normalized radiances around lunar aureole can be measured with a sky camera if it is configured to capture HDR images. Lunar almucantars from the camera have been compared with simulated radiances, obtaining a better fit between camera and model when the aerosol load is high and the Moon light is bright enough. The uncertainty of normalized camera radiance gets higher as the azimuth value goes farther from the Moon. This uncertainty is lower for MZA values from 30° to 40°, but it does not present a clear dependence on MZA. The camera normalized radiance uncertainty is 10% with an absolute bias around 1.0% and 1.5% for green and red channels, while the uncertainty of blue channel is 14% with an absolute bias of -3.2%. In general, the

normalized camera radiances fits the simulations better for the green (533 nm) and red (608 nm) channels.

GRASP code has the capability to include normalized radiances in the aerosol retrievals. The inversion of nocturnal AOD and normalized camera radiances together with GRASP could be used to study the aerosol properties evolution along the night, as it has been observed for a dust outbreak episode at Valladolid. In general, the obtained aerosol properties by GRASP at night fit well with the nearest diurnal properties provided by AERONET.

This work has demonstrated that normalized radiance near the lunar aureole can be detected by a sky camera, but, as a future work, the use of these normalized radiances in GRASP will need an exhaustive sensitivity study in order to ascertain which lunar aureole points provide more information, what aerosol properties can be retrieved with enough accuracy using this kind of measurements, and what are the best retrieval constraints.

## Acknowledgements

This work was supported by the Andalusia Regional Government (project P12-RNM-2409) and by the “Consejería de Educación” of “Junta de Castilla y León” (project VA100U14); the Spanish Ministry of Economy and Competitiveness and FEDER funds under the projects CGL2013-45410-R, CMT2015-66742-R, CGL2016-81092-R and “Juan de la Cierva-Formación” program (FJCI-2014-22052); and the European Union’s Horizon 2020 research and innovation programme through project ACTRIS-2 (grant agreement No 654109). The authors thankfully acknowledge the FEDER program for the instrumentation used in this work. The technical support given by Ying Li is acknowledged. The authors acknowledge the use of GRASP inversion algorithm ([www.grasp-open.com](http://www.grasp-open.com)). Tom Stone is also acknowledged for the ROLO calculations used in this work. The authors acknowledge the Consiglio Nazionale delle Ricerche of Italy for the purchase of the #918 (CE318-T) triple photometer within the Programma Operativo Nazionale (PONa3\_00363) I-AMICA, which in general operates at the University of Salento and was loaned to University of Granada for 3 months within the ACTRIS-2 research activities.



## References

- Alonso, J., Batlles, F.J., López, G., Ternero, A. (2014): Sky camera imagery processing based on a sky classification using radiometric data. *Energy*, 68, 599-608.
- Ansmann, A., Riebesell, M., and Weitkamp, C. (1990): Measurement of atmospheric aerosol extinction profiles with a Raman lidar. *Opt. Lett.* 15, 746–748.
- Ansmann, A., Wagner, F., Althausen, D., Müller, D., Herber, A., and Wandinger, U. (2001): European pollution outbreaks during ACE 2: Lofted aerosol plumes observed with Raman lidar at the Portuguese coast. *J. Geophys. Res.*, 106, 20725–20733.
- Barreto, A., Cuevas, E., Damiri, B., Berkoff, T., Berjón, A.J., Hernández, Y., Almansa, F., Gil, M. (2013): A new Method for nocturnal aerosol measurements with a lunar photometer prototype. *Atmos. Meas. Tech.*, 6, 585–598.
- Barreto, A., Cuevas, E., Granados-Muñoz, M.J., Alados-Arboledas, L., Romero, P.M., Gröbner, J., Kouremeti, N., Almansa, A.F., Stone, T., Toledano, C., Román, R., Sorokin, M., Holben, B., Canini, M., Yela, M. (2016): The new sun-sky-lunar Cimel CE318-T multiband photometer – a comprehensive performance evaluation. *Atmos. Meas. Tech.*, 9, 631–654.
- Barreto, A., Román, R., Cuevas, E., Berjón, A.J., Almansa, A.F., Toledano, C., González, R., Hernández, Y., Blarel, L., Goloub, P., Yela, M. (2017): Assessment of nocturnal Aerosol Optical Depth from lunar photometry at Izaña high mountain Observatory. *Atmos. Meas. Tech. Discuss.*, doi:10.5194/amt-2016-423.
- Benavent-Oltra, J.A., Román, R., Granados-Muñoz, M.J., Pérez-Ramírez, D., Ortiz-Amezcu, P., Denjean, C., Lopatin A., Lyamani, H., Torres, B., Guerrero-Rascado, J. L., Fuertes, D., Dubovik, O., Chaikovsky, A., Olmo, F.J., Mallet, M., Alados-Arboledas, L. (2017): Validation of GRASP code for a dust event over Granada (Spain) during ChArMEx/ADRIMED 2013 campaign. Submitted to *Atmos. Chem. Phys.*
- Berkoff, T.A., Sorokin, M., Stone, T., Eck, T.F., Hoff, R., Welton, E., Holben, B. (2011): Nocturnal aerosol optical depth measurements with a small-aperture automated photometer using the moon as a light source. *J. Atmos. Ocean. Tech.*, 28, 1297–1306, doi:10.1175/JTECH-D-10-05036.1.
- Bovchaliuk, V., Goloub, P., Podvin, T., Veselovskii, I., Tanre, D., Chaikovsky, A., Dubovik, O., Mortier, A., Lopatin, A., Korenskiy, M., Victori, S. (2016): Comparison of aerosol properties retrieved using GARRLiC, LIRIC, and Raman algorithms applied to multi-wavelength LIDAR and sun/sky-photometer data. *Atmos. Meas. Tech.*, 9, 3391-3405.
- Cachorro, V.E., Burgos, M.A., Mateos, D., Toledano, C., Bennouna, Y., Torres, B., de Frutos, A., Herguedas, A. (2016). Inventory of African desert dust events in the north-

central Iberian Peninsula in 2003–2014 based on sun-photometer–AERONET and  
particulate-mass–EMEP data. *Atmos. Chem. Phys.*, 16(13), 8227–8248.

Calbó, J., Sabburg, J. (2008): Feature extraction from whole-sky ground-based images  
for cloud-type recognition. *Journal of Atmospheric and Oceanic Technology*, 25(1), 3–  
14.

Cazorla, A., Olmo, F.J., Alados-Arboledas, L. (2008a). Development of a sky imager  
for cloud cover assessment. *J. Opt. Soc. Am. A*, 25(1), 29–39.

Cazorla, A., Olmo, F.J., Alados-Arboledas, L. (2008b): Using a Sky Imager for aerosol  
characterization. *Atmos. Environ.*, 42, 2739–2745,  
doi:10.1016/j.atmosenv.2007.06.016.

Cazorla, A., Husillos, C., Antón, M., Alados-Arboledas, L. (2015): Multi-exposure  
adaptive threshold technique for cloud detection with sky imagers. *Solar Energy* 114,  
268–277.

Cazorla, A., Casquero-Vera, J.A., Román, R., Guerrero-Rascado, J.L., Toledano, C.,  
Cachorro, V.E., Orza, J.A.G., Cancillo, M.L., Titos, G., Pandolfi, M., Alastuey, A.,  
Hanrieder, N., Alados-Arboledas, L. (2017): Near real time processing of ceilometer  
network data: Characterizing an extraordinary dust outbreak over the Iberian Peninsula.  
*Atmos. Chem. Phys. Discuss.*, doi:10.5194/acp-2017-151.

Chauvin, R., Nou, J., Thil, S., Grieu, S. (2015): Modelling the clear-sky intensity  
distribution using a sky imager. *Solar Energy*, 119, 1–17.

Debevec, P.E., Malik, J. (1997): Recovering high dynamic range radiance maps from  
photographs. *Proceedings of SIGGRAPH 97*, 369–378. ISBN 0-89791-896-7. Held in  
Los Angeles, California.

Dubovik, O., King, M. D. (2000): A flexible inversion algorithm for retrieval of aerosol  
optical properties from Sun and sky radiance measurements. *J. Geophys. Res. Atmos.*,  
105, 20673–20696.

Dubovik, O., Smirnov, A., Holben, B.N., King, M.D., Kaufman, Y.J., Eck, T.F.,  
Slutsker, I. (2000): Accuracy assessments of aerosol optical properties retrieved from  
Aerosol Robotic Network (AERONET) Sun and sky radiance measurements. *Journal of*  
*Geophysical Research: Atmospheres*, 105(D8), 9791–9806.

Dubovik, O., Sinyuk, A., Lapyonok, T., Holben, B.N., Mishchenko, M., Yang, P., Eck,  
T., Volten, H., Munoz, O., Veihelmann, B., Van Der Zande, W.J., Leon, J., Sorokin, M.,  
Slutsker, I. (2006): Application of spheroid models to account for aerosol particle  
nonsphericity in remote sensing of desert dust. *J. Geophys. Res. Atmos.*, 111, D11208.

Dubovik, O., Lapyonok, T., Litvinov, P., Herman, M., Fuertes, D., Ducos, F., Lopatin,  
A., Chaikovsky, A., Torres, B., Derimian, Y., Huang, X., Aspetsberger, M., Federspiel,

861 C. (2014): GRASP: a versatile algorithm for characterizing the atmosphere. SPIE:  
862 Newsroom 10.1117/2.1201408.005558.

863 Fedarenka, A., Dubovik, O., Goloub, P., Li, Z., Lapyonok, T., Litvinov, P., Blarel, L.,  
864 Gonzalez, L., Podvin, T., Crozel, D. (2016): Utilization of AERONET polarimetric  
865 measurements for improving retrieval of aerosol microphysics: GSFC, Beijing and  
866 Dakar data analysis. *J. Quant. Spectrosc. Radiat. Transfer*, 179, 72-97.

867 Fernald F.G. (1984): Analysis of atmospheric lidar observations: some comments. *Appl.*  
868 *Opt.* 23, 652–653.

869 Forster, B.C., Best, P. (1994): Estimation of SPOT P-mode point spread function and  
870 derivation of a deconvolution filter. *ISPRS Journal of Photogrammetry and Remote*  
871 *Sensing*, 49(6), 32-42.

872 Ghonima, M.S., Urquhart, B., Chow, C.W., Shields, J.E., Cazorla, A., Kleissl, J. (2012):  
873 A method for cloud detection and opacity classification based on ground based sky  
874 imagery. *Atmos. Meas. Tech.*, 5(11), 2881-2892.

875 González, Y., Lopez, C., Cuevas, E. (2012): Automatic observation of cloudiness:  
876 analysis of all sky images, TECO-2012, In: WMO Technical Conference on  
877 Meteorological and Environmental Instruments and Methods of Observation, Brussels,  
878 Belgium, 16–18 October 2012.

879 Haywood, J.M., Boucher, O. (2000): Estimates of the direct and indirect radiative  
880 forcing due to tropospheric aerosols: A review. *Rev. Geophys.*, 38, 513–543.

881 Holben, B.N., Eck, T.F., Slutsker, I., Tanré, D., Buis, J.P., Setzer, A., Vermote, E.,  
882 Reagan, J. A., Kaufman, Y. J., Nakajima, T., Lavenue, F., Jankowiak, I., Smirnov A.  
883 (1998): AERONET – A federated instrument network and data archive for aerosol  
884 characterization. *Remote Sens. Environ.*, 66, 1–16, 1998.

885 Holben, B. N., Eck, T. F., Slutsker, I., Smirnov, A., Sinyuk, A., Schafer, J., Giles, D.,  
886 Dubovik, O. (2006): AERONET's version 2.0 quality assurance criteria. *Proc. SPIE*  
887 6408, Remote Sensing of the Atmosphere and Clouds, 64080Q (November 28, 2006);  
888 doi:10.1117/12.706524.

889 Horváth, G., Barta, A., Gál, J., Suhai, B., Haiman, O. (2002): Ground-based full-sky  
890 imaging polarimetry of rapidly changing skies and its use for polarimetric cloud  
891 detection. *Appl. Optics*, 41, 543–559.

892 IPCC (Intergovernmental Panel on Climate Change) (2014): Climate Change 2014:  
893 Synthesis Report. Contribution of Working Groups I, II and III to the Fifth Assessment  
894 Report of the Intergovernmental Panel on Climate Change [Core Writing Team, R.K.  
895 Pachauri and L.A. Meyer (eds.)]. IPCC, Geneva, Switzerland, 151.

896 Kaufman, Y.J., Koren, I., Remer, L.A., Rosenfeld, D., Rudich, Y. (2005): The effect of  
897 smoke, dust, and pollution aerosol on shallow cloud development over the Atlantic  
898 Ocean. *Proc. Natl. Acad. Sci. USA*, 102, 11207–11212.

899 Kazantzidis, A., Tzoumanikas, P., Bais, A.F., Fotopoulos, S., Economou, G. (2012):  
900 Cloud detection and classification with the use of whole-sky ground-based images.  
901 *Atmos. Res.*, 113, 80-88.

902 Kholopov, G. K. (1975): Calculation of the effective wavelength of a measuring  
903 system. *J. Appl. Spectrosc.*, 23, 1146–1147, doi:10.1007/BF00611771.

904 Kieffer, H.H., Stone, T.C. (2005): The spectral irradiance of the moon. *Astronom. J.*,  
905 129, 2887–2901.

906 Klett J.D. (1981): Stable analytical inversion solution for processing lidar returns. *Appl.*  
907 *Opt.* 20, 211–220.

908 Klett J.D. (1985): Lidar inversion with variable backscatter/extinction ratios. *Appl. Opt.*  
909 24, 1638–1643.

910 Kokhanovsky, A.A., Davis, A.B., Cairns, B., Dubovik, O., Hasekamp, O.P., Sano, I.,  
911 Mukai, S., Rozanov, V.V., Litvinov, P., Lapyonok, T., Kolomiets, I.S., Oberemok,  
912 Y.A., Savenkov, S., Martin, W., Wasilewski, A., Di Noia, A., Stap, F.A., Rietjens, J.,  
913 Xu, F., Natraj, V., Duan, M., Cheng, T., Munro, R. (2015): Space-based remote sensing  
914 of atmospheric aerosols: The multi-angle spectro-polarimetric frontier. *Earth-Science*  
915 *Reviews*, 145, 85-116.

916 Kreuter, A., Zangerl, M., Schwarzmam, M., Blumthaler, M. (2009): All-sky imaging: a  
917 simple, versatile system for atmospheric research. *Appl. Optics*, 48, 1091–1097.

918 Lohmann, U., Feichter, J. (2005): Global indirect aerosol effects: A review. *Atmos.*  
919 *Chem. Phys.* 5, 715–737.

920 Long, C.M., Sabburg, J.M., Calbó, J., and Pagés, D. (2006): Retrieving cloud  
921 characteristics from ground-based daytime color all-sky images. *J. Atmos. Ocean.*  
922 *Tech.*, 23, 633–652.

923 Lopatin, A., Dubovik, O., Chaikovsky, A., Goloub, P., Lapyonok, T., Tanré, D.,  
924 Litvinov, P. (2013): Enhancement of aerosol characterization using synergy of lidar and  
925 sun-photometer coincident observations: the GARRLiC algorithm. *Atmos. Meas. Tech.*,  
926 6, 2065–2088, doi:10.5194/amt-6-2065-2013.

927 López-Álvarez, M., Hernández-Andrés, J., Romero, J., Olmo, F.J., Cazorla, A., and  
928 Alados-Arboledas, L. (2008): Using a trichromatic CCD camera for spectral skylight  
929 estimation. *Appl. Optics*, 47, 31–38.

930 Lyamani, H., Olmo F.J., Alados-Arboledas, L. (2010): Physical and optical properties  
 931 of aerosols over an urban location in Spain: seasonal and diurnal variability. *Atmos.*  
 932 *Chem. Phys.*, 10, 239–254.

933 Lyamani, H., Olmo, F.J., Foyo, I., Alados-Arboledas, L. (2011): Black carbon aerosols  
 934 over an urban area in south-eastern Spain: changes detected after the 2008 economic  
 935 crisis. *Atmos. Environ.* 45, 6423-6432.

936 Mandat, D., Pech, M., Hrabovsky, M., Schovanek, P., Palatka, M., Travnicek, P.,  
 937 Prouza, M., Ebr, J. (2014): All Sky Camera instrument for night sky monitoring. in  
 938 Proceedings of the First AtmoHEAD Conference, Saclay, June 10-12,  
 939 arXiv:1402.4762.

940 McGillem, C. D., Anuta, P. E., Malaret, E., Yu, K. B. (1983): Estimation of a remote  
 941 sensing system point-spread function from measured imagery. *LARS Technical*  
 942 *Reports*, 81.

943 McMurry, P.H. (2000): A review of atmospheric aerosol measurements. *Atmospheric*  
 944 *Environment* 34, 1959–1999.

945 NASA Facts (1999): Clouds and Energy cycle. Technical Report NF-207, NASA,  
 946 Goddard Space Flight Center, Maryland, USA.

947 O'Neill, N.T., Eck, T.F., Smirnov, A., Holben, B.N., Thulasiraman, S. (2003): Spectral  
 948 discrimination of coarse and fine mode optical depth. *J. Geophys. Res.*, 108 (D17),  
 949 4559. <http://dx.doi.org/10.1029/2002JD002975>.

950 Pinilla, C., Ariza, F.J., Peláez, J.A (1999), Obtención de la función de dispersión  
 951 puntual (PSF) en imágenes SPOT convencionales. Teledetección, VIII Spanish Remote  
 952 Sensing Meeting. Albacete (Spain), 403-406.

953 Pérez-Ramírez, D., Ruiz, B., Aceituno, J., Olmo, F.J., and Alados-Arboledas, L. (2008):  
 954 Application of Sun/star photometry to derive the aerosol optical depth. *Int. J. Remote*  
 955 *Sens.*, 29, 5113–5132, doi:10.1080/01431160802036425.

956 Pérez-Ramírez, D., Lyamani, H., Olmo, F.J., and Alados-Arboledas, L. (2011):  
 957 Improvements in star photometry for aerosol characterizations. *J. Aerosol Sci.*, 42, 737–  
 958 745, doi:10.1016/j.jaerosci.2011.06.010.

959 Ramanathan, V., Cess, R.D., Harrison, E.F., Minnis, P., Barkstrom, B.R. (1989): Cloud  
 960 radiative forcing and climate: results from the Earth radiation budget experiment.  
 961 *Science*, 243(4887), 57.

962 Ramanathan, V., Crutzen, P.J., Kiehl, J.T., Rosenfeld, D. (2001): Atmosphere—  
 963 Aerosols, climate, and the hydrological cycle. *Science*, 294, 2119–2124.

964 Reinhard, E., Stark, M., Shirley, P., Ferwerda, J. (2002). Photographic tone  
 965 reproduction for digital images. *ACM Transactions on Graphics (TOG)*, 21(3), 267-276.

966 Richardson, W.H. (1972): Bayesian-Based Iterative Method of Image Restoration. *J.*  
967 *Opt. Soc. Am.*, 62 (1), 55–59. doi:10.1364/JOSA.62.000055.

968 Lucy, L.B. (1974): An iterative technique for the rectification of observed distributions.  
969 *Astron. J.*, 79 (6), 745–754. doi:10.1086/111605.

970 Rodríguez, S., Alastuey, A., and Querol, X. (2012): A review of methods for long term  
971 in situ characterization of aerosol dust. *Aeolian Res.*, 6, 55–74,  
972 doi:10.1016/j.aeolia.2012.07.004.

973 Román, R., Antón, M., Cazorla, A., de Miguel, A., Olmo, F.J., Bilbao, J., Alados-  
974 Arboledas, L. (2012): Calibration of an all-sky camera for obtaining sky radiance at  
975 three wavelengths. *Atmos. Meas. Tech.*, 5, 2013–2024.

976 Román, R., Bilbao, J., and de Miguel, A. (2014a): Reconstruction of six decades of  
977 daily total solar shortwave irradiation in the Iberian Peninsula using sunshine duration  
978 records. *Atmos. Environ.*, 99, 41–50.

979 Román, R., Bilbao, J., and de Miguel, A. (2014b): Uncertainty and variability in  
980 satellite-based water vapor column, aerosol optical depth and Angström Exponent, and  
981 its effect on radiative transfer simulations in the Iberian Peninsula. *Atmos. Environ.*, 89,  
982 556–569.

983 Rosenfeld, D., Kaufman, Y.J., Koren, I. (2006): Switching cloud cover and dynamical  
984 regimes from open to closed Benard cells in response to the suppression of precipitation  
985 by aerosols. *Atmos. Chem. Phys.*, 6, 2503–2511.

986 Sasano, Y., Nakane H. (1984): Significance of the extinction/backscatter ratio and the  
987 boundary value term in the solution for the two-component lidar equation. *Appl. Opt.*,  
988 vol. 23, 11–13.

989 Sicard, M., Bertolín, S., Mallet, M., Dubuisson, P., Comerón, A. (2014): Estimation of  
990 mineral dust long-wave radiative forcing: sensitivity study to particle properties and  
991 application to real cases in the region of Barcelona. *Atmos. Chem. and Phys.*, 14(17),  
992 9213-9231.

993 Sigernes, F., Holmen, S.E., Biles, D., Bjørklund, H., Chen, X., Dyrland, M., Lorentzen,  
994 D.A., Baddeley, L., Trondsen, T., Brändström, U., Trondsen, E., Lybekk, B., Moen, J.,  
995 Chernouss, S., Deeher, C. S. (2014): Auroral all-sky camera calibration. *Geosci. Instrum.*  
996 *Method. Data Syst.*, 3, 241–245, 2014. doi:10.5194/gi-3-241-2014.

997 Stier, P., Seinfeld, J. H., Kinne, S., Boucher, O. (2007): Aerosol absorption and  
998 radiative forcing. *Atmos. Chem. Phys.*, 7(19), 5237-5261.

999 Stone, R.S., Herber, A., Vitale, V., Mazzola, M., Lupi, A., Schnell, R.C., Dutton, E.G.,  
1000 Liu, P.S.K, Li, S.-M., Dethloff, K., Lampert, A., Ritter, C., Stock, M., Neuber, R.,  
1001 Maturilli, M. (2010): A three-dimensional characterization of Arctic aerosols from

1002 airborne Sun photometer observations: PAM-ARCMIP, April 2009. *J. Geophys. Res.*,  
1003 115, D13203, doi:10.1029/2009JD013605.

1004 Mullikin, J.C., van Vliet, L.J., Netten, H., Boddeke, F.R., Van der Feltz, G., Young, I.T.  
1005 (1994): Methods for CCD camera characterization. *IS&T/SPIE 1994 International*  
1006 *Symposium on Electronic Imaging: Science and Technology*, 73-84. Stumpf, J.,  
1007 Tchou, C., Jones, A., Hawkins, T., Wenger, A., Debevec, P. (2004): Direct HDR  
1008 capture of the sun and sky. In *Proceedings of the 3rd international conference on*  
1009 *Computer graphics, virtual reality, visualisation and interaction in Africa* (pp. 145-149).  
1010 ACM.

1011 Tohsing, K., Schrempf, M., Riechelmann, S., Schilke, H., Seckmeyer, G. (2013):  
1012 Measuring high-resolution sky luminance distributions with a CCD camera. *Appl.*  
1013 *Optics*, 52(8), 1564-1573.

1014 Titos G, Foyo-Moreno I, Lyamani H, Querol X, Alastuey A, Alados-Arboledas L.  
1015 (2012): Optical properties and chemical composition of aerosol particles at an urban  
1016 location: An estimation of the aerosol mass scattering and absorption efficiencies, *J.*  
1017 *Geophys. Res.*, 117, D04206, doi:10.1029/2011JD016671,.

1018 Titos G., Lyamani H., Pandolfi M., Alastuey A., Alados-Arboledas L. (2014):  
1019 Identification of fine (PM<sub>1</sub>) and coarse (PM<sub>10-1</sub>) sources of particulate matter in an  
1020 urban environment. *Atmos. Environ.*, 89, 593-602.

1021 Tomasi, C., Kokhanovsky, A.A., Lupi, A., Ritter, C., Smirnov, A., O'Neill, N.T., Stone,  
1022 R.S., Holben, B.N., Nyeki, S., Wehrli, C., Stohl, A., Mazzola, M., Lanconelli, C.,  
1023 Vitale, V., Stebel, K., Aaltonen, V., de Leeuw, G., Rodriguez, E., Herber, A.B.,  
1024 Radionov, V.F., Zielinski, T., Petelski, T., Sakerin, S.M., Kabanov, D.M., Xue, Y. Mei,  
1025 L., Istomina, L., Wagener, R., McArthur, B., Sobolewski, P.S., Kivi, R., Courcoux, Y.,  
1026 Larouche, P., Broccardo, S., Piketh, S.J., Stohl, A. (2015): Aerosol remote sensing in  
1027 polar regions. *Earth-Sci. Rev.*, 140, 108-157.

1028 Torres, B., Dubovik, O., Fuertes, D., Lapyonok, T., Toledano, C., Schuster, G. L.,  
1029 Goloub, P., Blarel, L., Barreto, A., Mallet, M., Tanré, D. (2016): Advanced  
1030 characterization of aerosol properties from measurements of spectral optical depth using  
1031 the GRASP algorithm. *Atmos. Meas. Tech. Discuss.*, doi:10.5194/amt-2016-334.

1032 Urquhart, B., Kurtz, B., Dahlin, E., Ghonima, M., Shields, J. E., Kleissl, J. (2014):  
1033 Development of a sky imaging system for short-term solar power forecasting. *Atmos.*  
1034 *Meas. Tech.*, 8, 875–890, 2015.

1035 Voss, K.J., Zibordi, G. (1989): Radiometric and geometric calibration of a visible  
1036 spectral electro-optic “fisheye” camera radiance distribution system. *J. Atmos. Ocean.*  
1037 *Tech.*, 6, 652–662.

1038 Widenhorn, R., Blouke, M.M., Weber, A., Rest, A., Bodegom, E. (2002): Temperature  
1039 dependence of dark current in a CCD. Proc. SPIE, 4669, 193-201. Wild, M. (2012):  
1040 Enlightening global dimming and brightening. Bull. Amer. Meteor. Soc., 93, 27–37.

1041

1042

1043

1044

1045

1046

1047

1048

1049

1050

1051

1052

1053

1054

1055

1056

1057

1058

1059

1060

1061

1062

1063

1064

1065

1066



## List of Figure Captions

Figure 1: Spectral responses of the three channels (blue, green and red) of the CCD (panel a), of the infrared (IR) cut-off filter (panel b), and of the three channels of the camera (CCD plus infrared cut-off filter; panel c). The effective wavelengths of the camera for lunar applications are marked in panel c.

Figure 2: Zenith (panels a and b), Azimuth (panels c and d) and FOV (panels e and f) viewed by each camera pixel at Granada (panels a, c and e) and Valladolid (panels b, d and f). Azimuth is defined from 0° (North) to 360° being East 90° and West 270°.

Figure 3: Sensitivity of the camera pixels for each channel as a function of pixel counts for both Granada (panel a) and Valladolid (panel b) cameras. The shadow band around the lines represents the standard deviation.

Figure 4: Dark frames obtained with the Granada camera for different temperatures (T) and exposure times (ET). The signal shown is multiplied by 4 in order to be better appreciated.

Figure 5: Most frequent value in a dark frame as a function of temperature (T) and logarithm of the exposure time (ET), for the three Granada camera channels.

Figure 6: Non-HDR (upper; panels a, b and c) tone mapped sky images before removing background signal (middle; panels d, e and f) and tone mapped sky images with background corrected (bottom; panels g, h and i). Images corresponds to Granada 21<sup>st</sup> July 2016, 00:40UTC (left; panels a, d and g); Granada 20<sup>th</sup> May 2015, 21:25UTC (middle; panels b, e and h); Valladolid 3<sup>rd</sup> August 2015, 02:40UTC (right; panels c, f and i). The non-HDR image at Valladolid was taken under colorless conditions. Pixels with zenith angle above 80° are masked except for non-HDR images.

Figure 7: Determination coefficient ( $r^2$ ) between the background pixel signal and the AOD assumed at each channel. These values are shown for each channel at Granada (left) and Valladolid (right). Pixels with zenith angle above 80° are masked.

Figure 8: Averaged background HDR images obtained at Granada (panel a) and Valladolid (panel b). Images are not tone mapped and pixels with zenith angle above 80° are masked.

Figure 9: Normalized lunar almucantar radiances from camera (panel a) and simulated ones by GRASP (panel b) for Granada 21<sup>st</sup> July 2016, 00:40UTC. Panel c shows the ratio of normalized camera radiance to normalized GRASP radiance along the night 20<sup>th</sup>-21<sup>st</sup> May 2016 as a function of azimuth.

Figure 10: Normalized radiance from camera as a function of simulated by GRASP for 8 different nights at 469 nm (panel a), 533 nm (panel b) and 608 nm (panel c).

Figure 11: Box plots for the relative distribution of  $\Delta NR$  at 469 nm (panel a), 533 nm (panel b) and 608 nm (panel c) for different azimuth intervals. The box limits are the 25 and 75 percentiles, the error bar is the standard deviation, the circle is the mean, the red line inside the box is the median, the crosses are the 5 and 95 percentiles, and the triangles are the 1 and 99 percentiles.

1105 Figure 12: Box plots for the relative distribution of  $\Delta NR$  at 469 nm (panel a), 533 nm (panel b)  
 1106 and 608 nm (panel c) for different MZA intervals. The box limits are the 25 and 75 percentiles,  
 1107 the error bar is the standard deviation, the circle is the mean, the red line inside the box is the  
 1108 median, the crosses are the 5 and 95 percentiles, and the triangles are the 1 and 99 percentiles.

1109 Figure 13: Spectral AOD (panel a) and Angström Exponent (panel b) at day and night from 2<sup>nd</sup>  
 1110 to 3<sup>rd</sup> August 2015 at Valladolid. Crosses and points represent nocturnal and diurnal data,  
 1111 respectively.

1112 Figure 14: Evolution of the real (panel a) and imaginary (panel b) refractive indices, sphere  
 1113 fraction (panel c) and SSA (panel d) at Valladolid from 2<sup>nd</sup> to 3<sup>rd</sup> August 2015. Diurnal values  
 1114 retrieved by AERONET are represented as circles, while nocturnal values retrieved by GRASP,  
 1115 using normalized camera radiances and nocturnal AOD, are represented by crosses with their  
 1116 error bars.

1117 Figure 15: Parameters of the fine (panels a, c and e) and coarse (panels b, d and f) aerosol size  
 1118 distributions from AERONET (black circles) and from GRASP retrieval using normalized  
 1119 camera radiances and nocturnal AOD (blue crosses with error bars) at Valladolid from 2<sup>nd</sup> to 3<sup>rd</sup>  
 1120 August 2015.